

DEVELOPMENT OF HIGH QUANTUM EFFICIENCY STRAINED SUPERLATTICE
SPIN POLARIZED PHOTOCATHODES VIA METAL ORGANIC CHEMICAL VAPOR
DEPOSITION

By

Benjamin Belfore

B.S. May 2016 Virginia Polytechnic Institute and State University

A Dissertation Submitted to the Faculty of Old Dominion University in Partial Fulfillment
of the Requirements for the Degree of
DOCTOR OF PHILOSOPHY

ENGINEERING

OLD DOMINION UNIVERSITY

JUNE 2022

Approved by:

Sylvain Marsillac (Director)

Orlando Ayala (Member)

Dimitrie Popescu (Member)

Linda Vahala (Member)

ABSTRACT

Spin polarized photocathodes are necessary to examine parity violations and other fundamental phenomena in the field of high energy physics. To create these devices, expensive and complicated growth processes are necessary. While integral to accelerator physics, spin polarized electrons could have other exciting applications in materials science and other fields of physics. In order to explore these other applications feasibly, the relative supply of spin polarized photocathodes with a high rate of both polarization and photoemission needs to be increased. One such way to increase this supply is to develop the means to grow them faster and at a larger scale. Because most photocathodes are grown in slow, small-scale processes like Molecular Beam Epitaxy, an alternative needed to be found. In the following work, strained superlattice photocathodes were fabricated using metal organic vapor phase epitaxy. Using this growth process, we demonstrated that it is possible to create high quality photocathodes at a higher rate while maintaining a high quality of polarization and quantum efficiency, thus allowing for the exploration of other applications for these devices.

Copyright, 2022, by Benjamin Belfore, All Rights Reserved

ACKNOWLEDGEMENTS

I would first like to thank the people at various universities and labs that made this work possible. In particular, I would like to thank Dr. Seth Hubbard and Dr Stephen Polly at Rochester Institute of Technology. Their expertise in MOCVD growth of III-V materials was invaluable to the success of this project. I would also like to thank the scientist at both Jefferson National Lab and Brookhaven National Lab. At Jefferson Lab, I would particularly like to thank Dr. Mother Poelker for being very supportive of this project and being a wellspring of knowledge that was invaluable of shaping this project. At Brookhaven, I would like to thank Dr. Erdong Wang and Dr. Wei Liu the polarization measurements done were performed by them and were invaluable.

At Old Dominion University, there are so many people I would like to thank. My advisor Dr. Sylvain Marsillac continued to challenge me for my entire time here, for that I am grateful, and Dr. Orlando Ayala was not only a committee member and colleague but also a mentor and confidant. The remainder of my committee, Dr. Dimitrie Popescu and Dr. Linda Vahala were exceedingly patient and understanding. My work would have been so much more difficult if it weren't for Lori Barret and Romina Samson. They were key to enabling my success during my time here.

Finally, I would like to thank my parents Lee and Renee Belfore. They were a continual source of motivation and are responsible for the person I am today. They gave me a framework that allowed me to be successful and fostered a curiosity in me that made me the successful engineer I am today

Table of Contents

Chapter 1: Device and Physics Overview	7
1.1 Introduction	7
1.2 History of Spin Polarized Electron Sources	8
1.3 Electron Affinity and Photo Emission.....	13
Chapter 2: MOCVD Growth and Characterization	16
2.1 Introduction	16
2.2 Defects	17
2.3 III-V Background.....	19
2.4 MOCVD Growth Process	20
2.5. Growth Characterization.....	23
2.5.1 Pyrometry	25
2.5.2 <i>Curvature</i>	26
2.5.3 Surface reflectivity	27
2.6. Post Growth Characterization.....	27
2.6.1 Nomarski Microscopy	28
2.6.2 X-Ray Diffraction	30
2.6.3 Spectroscopic Ellipsometry	32
2.6.4 Transmission Electron Microscopy	35
2.6.5 Atomic Force Microscopy	38
2.6.6 Hall Effect	39
2.6.7 Device Testing	40
Chapter 3: Composition Calibrations and Metamorphic Grading Optimization	48
3.1. Introduction	48
3.2. Composition calibrations for GaAs _x P _{1-x}	49
3.3. Metamorphic layer calibration	53
3.4. Metamorphic layer optimization	56
Chapter 4: Superlattice Growth and Device Characterization.....	65
4.1. Introduction	65
4.2. GaAs/GaAs _{0.65} P _{0.35} superlattice growth.....	65
4.3. Initial device characterization.....	67
4.4. Device Refinement.....	68

4.5. Distributed Bragg Reflector.....	74
Conclusion.....	81
References	82

LIST OF TABLES

TABLE 1 RESULTS OF SINGLE LAYER GAAsP GROWTHS	51
TABLE 2: SUMMARY OF METAMORPHIC GRADES GROWN DURING CALIBRATION WITH TARGETED PROPERTIES	53
TABLE 3 PHOTOCATHODE RESULTS COMPARED TO OTHER WORKS	78

LIST OF FIGURES

FIGURE 1.1 BAND STRUCTURE (LEFT) AND OPTICAL SPIN POLARIZATION DIAGRAM (RIGHT) FOR UNSTRAINED GAAs (EG: BAND GAP; LH: LIGHT HOLES; HH: HEAVY HOLES; Δ : DIFFERENCE OF ENERGY BETWEEN THE TOP BAND OF THE VALENCE BAND AND THE NEXT BAND) DERIVED FROM [6]	8
FIGURE 1.2 BAND STRUCTURE (LEFT) AND OPTICAL SPIN POLARIZATION DIAGRAM (RIGHT) OF GAAs UNDER COMPRESSIVE STRAIN DERIVED FROM [6]	10
FIGURE 1.3 EVOLUTION OF SPIN POLARIZED PHOTOCATHODES FROM LEFT TO RIGHT ARE: (1) GAAs WAFER, (2) STRAINED LAYER ON SUBSTRATE, (3) STRAINED LAYER WITH BUFFER LAYER, (4) STRAINED SUPERLATTICE AND (5) STRAINED SUPERLATTICE WITH DISTRIBUTED BRAGG REFLECTOR (NOT TO SCALE)	11
FIGURE 1.4 BAND DIAGRAM OF PHOTOEMISSION FROM PARTIALLY SURFACE TREATED GAAs [13]	13
FIGURE 1.5 BAND DIAGRAM OF PHOTOEMISSION WITH A NEGATIVE ELECTRON AFFINITY SURFACE [13]	14
FIGURE 1.6 EXAMPLE OF THE GENERATION OF A NEGATIVE ELECTRON AFFINITY SURFACE ILLUSTRATED BY THE EVOLUTION OF ELECTRON CURRENT WITH TIME.	15
FIGURE 2.1 CRYSTAL SYSTEM SHOWING THREE TYPES OF LOW DIMENSIONALITY DEFECTS: VACANCY (DASHED CIRCLE) INTERSTITIAL (BLUE CIRCLE) AND THREADING DISLOCATION (BLACK TO RED)	17
FIGURE 2.2 TEM IMAGE OF A MISFIT LINEAR DEFECT IN AN MOCVD-GROWN DBR	18
FIGURE 2.3 PLOT OF LATTICE CONSTANT VS BAND GAP OF ALL NON-NITRIDE III-V SEMICONDUCTORS DERIVED FROM [18]	19
FIGURE 2.4 MOCVD SYSTEM USED FOR OUR GROWTHS.	21
FIGURE 2.5 SCHEMATIC OF SIMPLIFIED GROWTH PROCESS IN MOCVD.	22
FIGURE 2.6 EXAMPLE OF GROWTH TELEMETRY FOR AN MOCVD PROCESS. THE PLOT SHOWS TEMPERATURE (RED), REFLECTIVITY (BLUE) AND CURVATURE (GREEN)	25
FIGURE 2.7 EXAMPLE OF HOW LATTICE MISMATCH OF GROWN FILM AND SUBSTRATE CAN CREATE CURVATURE (HIGHLY EXAGGERATE FOR DEMONSTRATION PURPOSES).	26
FIGURE 2.8 EXAMPLE OF NOMARSKI MICROSCOPY IMAGE OF METAMORPHIC GRADING	29
FIGURE 2.9 NOMARSKI OF LAYERS WITH 3 DIFFERENT QUALITIES OF EPITAXY. LEFT: GAAs _{0.95} PO _{0.05} MINIMAL STRAIN IN THE GROWN LAYERS SO MINIMAL SURFACE FEATURES; MIDDLE: TEXTURED PHOTOCATHODE; RIGHT: POORLY RELAXED GROWTH.	29
FIGURE 2.10 BASIC EXAMPLE OF THE BRAGG CONDITION	30
FIGURE 2.11 THREE DIFFERENT RECIPROCAL SPACE MAPS SHOWING METAMORPHIC GRADES OF 3 DIFFERENT STRAINS.	32
FIGURE 2.12 EXAMPLE OF RAW ELLIPSOMETRY DATA MEASURED ON A GAAs WAFER.	34
FIGURE 2.13 THE DETECTOR SCHEME FOR A HAADF (DERIVED FROM [30]) SYSTEM ALONGSIDE TWO HAADF IMAGES SHOWING ATOMIC-SCALE RESOLUTION	36
FIGURE 2.14 EXAMPLE OF DIFFRACTION PATTERN AND ANALYSIS FOR ONE OF OUR SAMPLES ALONG WITH A SAMPLE SHOWING THE RECIPROCAL SPACE VECTORS	37
FIGURE 2.15 EXAMPLE OF EDS MAPPING OF THE VARIOUS ELEMENTS WITHIN THE DBR	38
FIGURE 2.16 EXAMPLE OF AN AFM IMAGE ON ONE OF OUR SAMPLES	39
FIGURE 2.17 THE MOTT POLARIMETER 1: THE MOUNTING STALK 2: UHV ISOLATION VALVE 3: CESIUM HEAT SOURCE 4: NF ₃ LEAK VALVE 5: LASER OPTICS 6: MOTT POLARIMETER	41
FIGURE 2.18 PHOTOCATHODE MOUNTED ON THE MOLYBDENUM STALK WITH THE TANTALUM PRESS CONTACT.	42
FIGURE 2.19 IMAGE ILLUSTRATING THE ACTIVATION PROCESS (ANODE CURRENT, TARGET CURRENT AND TRANSMISSION)	43
FIGURE 2.20 ILLUSTRATION OF THE ELECTRON OPTICS USED TO DIRECT THE ELECTRON BEAM TO THE MOTT DERIVED FROM [33].	45
FIGURE 2.21 IMAGE OF TUNABLE WHITE LIGHT LASER WITH POLARIZING AND FILTERING OPTICS	46
FIGURE 2.22 SCHEMATIC OF THE MOTT POLARIMETER DERIVED FROM [33].	46
FIGURE 3.1 IMAGES FROM NOMARSKI MICROSCOPY OF THE 3 DIFFERENT GAAs _x P _{1-x} COMPOSITION FILMS (PHOSPHOROUS CONTENT INCREASING FROM 0.05, TO 0.20 TO 0.35 FROM LEFT TO RIGHT).	49

FIGURE 3.2 COUPLED X-RAY DIFFRACTION MEASUREMENTS ON THREE GAASXP1-X FILMS (PHOSPHOROUS CONTENT INCREASING FROM 0.05, TO 0.20 TO 0.35 FROM LEFT TO RIGHT)	50
FIGURE 3.3 ELLIPSOmetry DATA OF THE THREE DIFFERENT GROWN GAASXP1-X SAMPLES	51
FIGURE 3.4 COMPLEX DIELECTRIC CONSTANT FOR GAASXP1-X FILM, WITH PHOSPHOROUS COMPOSITION RANGING FROM 0.05 TO 0.35. THE 0.35 SAMPLE SHOWS THE FULL DECONVOLUTION OF THE OSCILLATORS	52
FIGURE 3.5 COMPLEX DIELECTRIC CONSTANT OF THE THREE MODEL FILMS WITH REFERENCE MEASUREMENTS FOR GAAS AND GAP.....	52
FIGURE 3.6 RECIPROCAL SPACE MAPPING FOR THE INITIAL METAMORPHIC LAYER CALIBRATION (21R100)	54
FIGURE 3.7 GAS RATIO AS A FUNCTION OF PHOSPHOROUS COMPOSITION IN THE SOLID FOR VARIOUS SUBSTRATES TEMPERATURE AS EXTRACTED FROM TWO DIFFERENT METAMORPHIC GRADING RUNS (21R200 AND 21R201).....	55
FIGURE 3.8 TELEMETRY, HRXRD AND NOMARSKI RESULTS FOR A WAFER (LEFT) WITH 1O OFFCUT IN THE (110) DIRECTION AND (RIGHT) ON AXIS (21R100).....	57
FIGURE 3.9 TELEMETRY, HRXRD AND NOMARSKI RESULTS FOR GROWTH OFFCUT WAFER IN 21R201	58
FIGURE 3.10 TELEMETRY, HRXRD AND IMAGE RESULTS FOR OFFCUT WAFER IN 21R270	60
FIGURE 3.11 PHOTOLUMINESCENCE MAPPING FOR THE SAMPLE SHOWN IN FIGURE 3.10 THE HEAT MAP SHOWS THE AVERAGE PL INTENSITY.....	61
FIGURE 3.12 TELEMETRY, HRXRD, OPTICAL IMAGE, NOMARSKI IMAGE AND SEM RESULTS FOR THE OFFCUT WAFER IN 21R277	62
FIGURE 3.13 NOMARSKI AND RSM OF RUN 21R327 METAMORPHIC GRADINGS WITH (111) OFFCUT (LEFT) AND ON-AXIS (RIGHT)	63
FIGURE 4.1 XRD OF TWO GAAS/GAAS0.65P0.35 SUPERLATTICES GROWN ON (100) GAAS ON-AXIS (TOP) AND ON-AXIS WITH 2 DEGREE OFFCUT IN THE (110) DIRECTION (BOTTOM).....	66
FIGURE 4.2 ELECTRON SPIN POLARIZATION AND QUANTUM EFFICIENCY AS A FUNCTION OF WAVELENGTH FOR OUR INITIAL DEVICE (RUN# 21R333).....	67
FIGURE 4.3 TRANSMISSION ELECTRON MICROSCOPY OF THE SUPERLATTICE ON THE FIRST FULLY COMPLETED DEVICE (TOP) COMPARED TO A SAMPLE SUPERLATTICE GROWN ON ON-AXIS GAAS (BOTTOM)	69
FIGURE 4.4 ATOMIC FORCE MICROSCOPY IMAGE OF THE SUPERLATTICE ON TOP OF A FULL DEVICE WITH OFFCUT WAFER (COPY OF RECIPE FROM RUN #21R333).....	70
FIGURE 4.5 ATOMIC FORCE MICROSCOPY IMAGE OF THE SUPERLATTICE ON TOP OF A FULL DEVICE WITH ON-AXIS WAFER (RUN22R064)	71
FIGURE 4.6 NOMARSKI IMAGE AND ATOMIC FORCE MICROSCOPY IMAGE OF IMPROVED SUPERLATTICE PHOTOCATHODE (RUN 22R064).....	72
FIGURE 4.7 TEM IMAGING AND EDS ON PHOTOCATHODE WITH ON-AXIS WAFER (RUN 22R064)	73
FIGURE 4.8 ELECTRON SPIN POLARIZATION AND QUANTUM EFFICIENCY AS A FUNCTION OF WAVELENGTH FOR IMPROVED SUPERLATTICE PHOTOCATHODE (RUN 22R064)	73
FIGURE 4.9 GROWTH TELEMETRY OF DBR CONTAINING PHOTOCATHODE (RUN # 22R065).....	76
FIGURE 4.10 NOMARSKY IMAGE AND OPTICAL IMAGE OF PHOTOCATHODE WITH DBR (RUN 22R065).....	76
FIGURE 4.11 REFLECTIVITY MEASUREMENT AS A FUNCTION OF WAVELENGTH FOR A DBR DEPOSITED ON A METAMORPHIC LAYER	77
FIGURE 4.12 TWO DIFFERENT PHOTOCATHODES WITH THE SAME SUPERLATTICE RECIPE WITHOUT DBR (22R064, LEFT) AND WITH DBR (22R065, RIGHT).....	78
FIGURE 4.13 TEM IMAGING OF THE DBR FROM THE PREVIOUSLY REPORTED DEVICE WITH ADDITIONAL MAGNIFICATION ON THE DISLOCATION (22R065)	79
FIGURE 4.14 IMPACT OF MISFIT DISLOCATION CAUSED MY LATTICE MISMATCH IN THE DBR PROPAGATING INTO THE SUPERLATTICE (RUN22R065)	80

Chapter 1: Device and Physics Overview

1.1 Introduction

The future of accelerator physics is highly dependent on the availability of high intensity and highly-polarized electron sources. As physicist try to probe even more sensitive phenomena, the number of electrons that must be excited and the polarization of these electrons must be further increased. Unfortunately, sourcing these components is difficult. This is predominantly due to the lack of demand for these components outside of accelerator physics and the high cost of manufacturing said components. If the availability of such electron sources were increased, it could be possible to examine even more specialized physics. One area of potential interest to physicists is examining parity violations within the Q_{weak} force [1]. Outside of the field of accelerator physics, if these sources became more readily available, applications to other fields of science and engineering may become available. Characterization techniques that utilize spin polarized electrons are unique in that they can explore the magnetic properties of materials in unique ways through techniques like Spin Polarized Electron Back Scattering Diffraction (SPEBSD) [2]. To an even greater extent, if such sources were plentiful, new types of physical phenomena could be observed using spin polarized positrons. One area of exploration of particular interest is Polarized Electrons for Polarized Positrons (PEPO). To generate these polarized positrons, a significant number of polarized electrons must be generated [3]. By developing a reliable way to generate these spin polarized photocathodes, an entire new branch of physics could be explored.

One of the unique challenges for high-quantum efficiency spin polarized photocathodes is the growth process. Traditionally these devices have been grown via Molecular Beam Epitaxy (MBE) [4]. MBE allows for excellent growth control at the cost of deposition speed and price. One way to potentially increase the availability of these photocathodes is transition to a new growth process. A significant number of early photocathodes were grown via Metal Organic Chemical

Vapor Deposition (MOCVD). Due to many growth processes in MOCVD being controlled by chemical reaction kinetics, there are more limitations in chamber growth temperature and pressure. While these tradeoffs can potentially be an issue, MOCVD growth processes are significantly quicker and, generally, more versatile. MOCVD is also more viable for industrial scale up compared to MBE. Being able to transition high quantum efficiency spin polarized photocathodes from MBE to MOCVD would be a significant boon for the development of sciences that are dependent on the availability of spin polarized photocathodes.

1.2 History of Spin Polarized Electron Sources

Spin polarized electron sources have been integral to electron accelerators. Since the first demonstration spin polarized emission in 1976, significant effort has been put into developing these photocathodes for accelerator applications [5]. For that reason, their development has gone hand and hand with accelerator development. Initial spin polarized photocathodes were created using commercially available p-type GaAs wafers. Because of the band structure of GaAs, it is an excellent candidate for a photocathode (Figure 1.1).

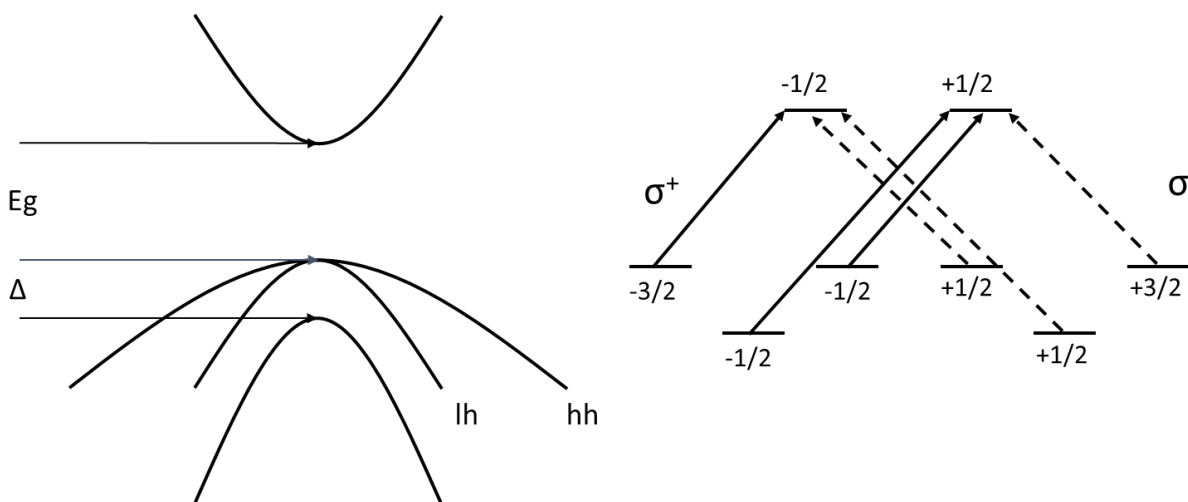


Figure 1.1 Band Structure (left) and optical spin polarization diagram (right) for unstrained GaAs (E_g : band gap; lh: light holes; hh: heavy holes; Δ : difference of energy between the top band of the valence band and the next band) derived from [6]

Figure 1.1 shows the band structure of GaAs at the band gap. Spin polarization emission can occur when circularly polarized light is absorbed in the region above the band gap but below Δ . Spin polarized electrons are then generated by the absorption of circularly polarized laser light. In the case of unstrained GaAs, one direction of polarization will only excite the solid arrows and the other will excite the dashed lines. The goal then is to excite only the top 4 orbitals. To determine the polarization of the electrons, the following formula is used:

$$P = \frac{N \uparrow - N \downarrow}{N \uparrow + N \downarrow} \quad (1)$$

where N is the number of electrons emitted and the arrow refers to the direction of the spin. Based on the orbital excitation shown in Figure 1, regardless of the direction of the polarized light, at most, 3 of 1 spin will be excited and 1 of the opposite spin will be. This results in a maximum theoretical spin polarization of 50% [4].

The other key parameter examined for spin polarized photocathodes is Quantum Efficiency (QE). QE can be summarized as the ratio of incoming photons (from the laser light) to emitted electrons. The quantum efficiency in a bulk photocathode is mainly affected by 3 properties: the incident photon wavelength, the thickness of the emitting area and the electron affinity of the surface. While discussed in greater detail in later chapters, specific surface treatments are performed to ensure photoemission at relatively low photon energies. Because there is no variance of composition within the GaAs wafer, photoemission can occur through the entire region where photoemission is possible (this region will be discussed in greater detail in the device physics section). Since physicist care about both QE and polarization, a metric had to be developed to quantify photocathodes of varying quality. The figure of merit used for these spin polarized photocathodes is P^2QE , where P denotes polarization and QE the quantum efficiency [4].

While GaAs photocathodes may have QEs in the range of 30% (which is good), 50% spin polarization is insufficient for most physics, so a new solution needed to be developed. Unfortunately, this maximum efficiency for the polarization is determined inherently by the band structure of GaAs. In order to improve spin polarization, either the properties of GaAs needed to be modified or a new material would need to be used. One way to modify the band structure of a material is to strain the bonds within the lattice. As the bond length changes, the energies of the band gap and other transitions will change. For the case of GaAs, when under compressive strain, the heavy hole and light hole bands at the band gap will split allowing the opportunity to excite potentially fewer bands (Figure 2) [6,7].

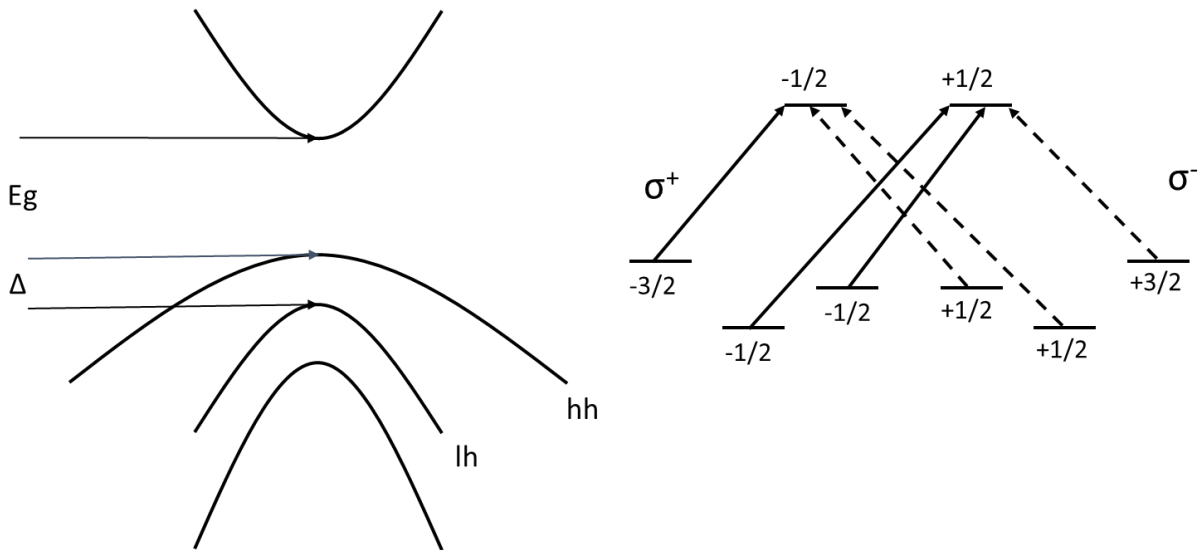


Figure 1.2 Band Structure (left) and optical spin polarization diagram (right) of GaAs under compressive strain derived from [6]

As Figure 1.2 shows, when GaAs is under compressive strain, the heavy hole and light hole bands, which previously were aligned at the band gap, split into two discrete bands. This allows, with precise control of the incident light energy, polarizations potentially up to 100%.

This band splitting phenomena was first proven using InGaAs layer on GaAs wafer. Growing a 100 nm thick layer on GaAs, a polarization of 70% was reached [8]. This innovation did not come without distinct challenges. One of the limiting factors of this process has to do with relaxation of

strain through a grown film. When a film thickness surpasses a critical thickness, the film will begin to relax (lose the strain). This results in the formation of defects and an overall poor-quality film. After this innovation, spin polarizations of over 90% were reached by growing a GaAs layer on a GaAsP buffer layer, but the quantum efficiency of these photocathodes was still poor [5]. There were multiple reasons for this low quantum efficiency, but one of the main problems was recombination due to defect formation during film relaxation. The lattice mismatch required to reach high levels of spin polarization requires layers of such high strain that critical thickness is on the scale of around 10 nm [9]. While defects do not form instantly when thickness past this are reached, defects will form in a 100 nm film. Not only does this relaxation result in defects and recombination, but since the strain is changing, the orbital splitting energy is changing. Because of this gradient in the orbital splitting energy, the wavelength of peak polarization will change, thus the maximum polarization will be lowered.



Figure 1.3 Evolution of Spin Polarized Photocathodes from left to right are: (1) GaAs Wafer, (2) Strained Layer on Substrate, (3) Strained layer with buffer later, (4) Strained Superlattice and (5) Strained Superlattice with Distributed Bragg Reflector (not to scale)

To address this issue a new device structure was developed (Figure 1.3). The goal of this new structure is to maintain strain through the entire device thickness. This is done by growing thin layers of emitting material in between layers of a buffer material. By growing such a superlattice, the emitting layer will maintain its strain as long as its thickness is below that of the critical thickness. With this new structure, the emitting material would not relax resulting in uniform strain and minimal defect formation. Initial InGaAs/GaAs superlattice structures resulted in polarizations of 82% with quantum efficiencies near 0.015% [10]. While the quantum efficiency was still low, both the spin polarization and quantum efficiency showed noticed increase over a strained epi-

layer InGaAs on GaAs. Much like in the strained epilayer system, when the materials were changed from InGaAs/GaAs to GaAsP/GaAs, both the spin polarization and quantum efficiency were improved. This improvement continued until photocathodes were developed with polarizations of 92% and quantum efficiencies of 1.6% [4].

While this high degree of polarization is excellent, the quantum efficiency would be ideally higher. Quantum efficiency is limited by multiple factors. First, while the superlattice does facilitate uniform strain through the emitting material, this barrier material in the superlattice does not emit spin polarized electrons. This results in around half of the emitting thickness emitting no electrons. Furthermore, carefully controlling the barrier thickness is integral to prevent depolarization. Transport from within the photocathode to the surface itself can cause depolarization, so a balance must be made between the thickness of both the buffer layer and the number of periods in the superlattice [4].

Now that the problem of high polarization has been solved, the challenge of improving quantum efficiency must be resolved. In opto-electronic devices, there are multiple ways to improve quantum efficiency. Some of these are surface specific like surface texturing and anti-reflective coatings. For photocathode application, neither of these processes are viable. While surface texturing will facilitate less light reflecting off the photocathode surface, the scattering of light at the surface would change the polarization of the light propagating through the photocathode. Even slight changes in the circularly polarized light will cause a drop in polarization. To successfully emit electrons from the photocathode surface, specific surface treatments must be performed; this prevents the use of antireflective coatings like MgF_2 [11]. This limits the way to improve quantum efficiency to increasing the device's active area thickness. As discussed previously, if the number of the periods of the superlattice is too high, depolarization during diffusion to the surface will occur and a drop in spin polarization will occur. To increase the thickness of the strained superlattice without changing its spatial dimensions, a Distributed Bragg Reflector (DBR) can be implemented. A DBR is a special type of dielectric mirror where materials of alternating

refractive indices are used to create a bandwidth with a high degree of reflectivity [12]. This results in all of the light that is not absorbed by the superlattice to be reflected back into the superlattice allowing for a second pass of laser light without actually increasing the active layer thickness. With the implementation of a DBR, photocathodes were developed with spin polarizations of 84% and a QE of 6.4% [4].

1.3 Electron Affinity and Photo Emission

Colloquially, electron affinity is the amount of energy released when a bond breaks in the gaseous phase. In solid state physics, a more specific definition exists. Within solid state physics, electron affinity is the difference between the conduction band energy and the vacuum level for a given material. Generally, this is considered a stable, bulk, material property. However, at the vacuum material interface, electron affinity is highly sensitive to the surface dipoles terminating on the surface. The previous section illustrated various band diagrams that showed that the region where spin polarization occurs is relatively narrow. The energy of the incident photons is slightly above the band gap of GaAs (1.42 eV). The electron affinity of GaAs is 4.07 eV, so photons that emit highly polarized electrons (energies around 1.58 eV) will not emit freely.

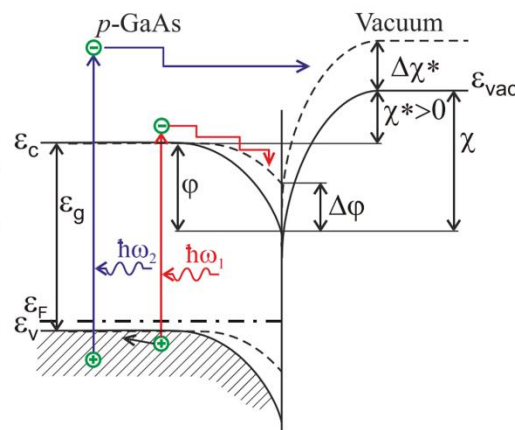


Figure 1.4 Band diagram of photoemission from partially surface treated GaAs [13]

In Figure 1.4, ϵ_g is the band gap, ϵ_c is the conduction band, ϵ_v is the valence band, ϵ_f is the fermi level, $h\omega$ are two photons of varying energy, ϕ shows the band bending energy, $\Delta\phi$ shows the

photovoltage impact on the band bending region, χ is the electron affinity, χ^* is the effective electron affinity, $\Delta\chi^*$ is the difference between the vacuum level and the effective electron affinity. Figure 1.4 shows that, in most cases, electrons excited from near the band gap will not emit from the surface, and only electrons with substantially higher energies will be able to emit freely from the surface. However, these higher energy electrons will not be properly polarized.

To successfully emit the electrons in the proper energy region, certain properties of the grown layers must be controlled. First, the entire photocathode must be p-type. A p-type material will facilitate more band bending at the surface of the material. This is because, at a material interface, the vacuum level will bend to the work function of a material. For a semiconductor, the energy of the Fermi level is the work function. The next modification that can be done to potentially allow for lower energy electrons to photoemit is to further lower the barrier at the interface. Since electron affinity at the surface is highly sensitive to surface dipoles, creating a large surface dipole would be ideal to further lowering the barrier of photoemission [13].

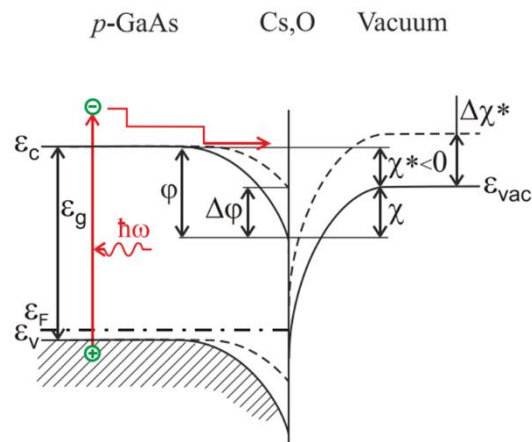


Figure 1.5 Band Diagram of photoemission with a negative electron affinity surface [13]

To create a negative electron affinity surface, a surface dipole is generated (Figure 1.5). This generation is done by depositing a sub-monolayer of cesium then a chemisorbed oxidation agent. This creates a surface dipole that allows the photoemission of these lower energy electrons.

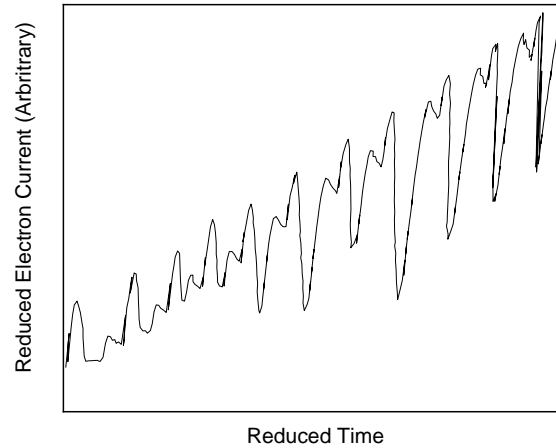


Figure 1.6: Example of the generation of a negative electron affinity surface illustrated by the evolution of electron current with time.

Figure 1.6 shows how surface treatment of a GaAs photocathode increases photoemission. By pulsing Cs and NF_3 (the oxidation agent used), the surface dipole is created. As the surface dipole becomes stronger during the activation process, the electron current increases. After the surface is sufficiently activated, it can be used to generate spin polarized electrons.

Chapter 2: MOCVD Growth and Characterization

2.1 Introduction

Two key technologies are used to grow high quality epitaxial films. These two techniques are Metal Organic Chemical Vapor Deposition (MOCVD) and Molecular Beam Epitaxy (MBE). While MOCVD is discussed in more detail in a subsequent section, understanding how both of them work, and why MOCVD was chosen over MBE, is key.

Molecular Beam Epitaxy is a deposition technique where precursor elements (typically pure, solid forms of the material) are heated until they are vaporized. It was developed pioneered by John Arthur and Alfred Cho at Bell Laboratories with the expressed purpose of depositing high quality III-V compound semiconductors [14]. To grow sufficiently high quality films, the deposition chamber is kept at a UHV condition ($\sim 1 \times 10^{-10}$ torr base pressure). Such low base pressures allow for minimal pollution from gas phase pollutants like water vapor. These lower pressures also allow for lower temperatures for the sources to mitigate potential outgassing. With such low chamber pressures, precise control of temperature and molecular flux can be obtained, and, with the development of other technologies like gas crackers to prevent the formation of gas phase allotropes, MBE is often the deposition method of choice for laboratory-scale setups [15].

While MBE has many distinct advantages, MOCVD provides multiple unique advantages that are ideal for specific growths. Instead of using elemental precursors, MOCVD use chemical precursors. That result in the deposition process being more dependent on the kinetic (reaction) processes during the deposition instead of pure molecular flux. These precursors are introduced via either temperature controlled baths with a hydrogen carrier gas flow or directly from gas sources. This allows specific and precise control of the chemical precursors into the reaction chamber. While the finer points of MOCVD will be discussed in detail later, since the growth rate

processes are dependent on the growth surface temperature and flux of vapor phase precursor, reproducibility run-to-run variance are minimized. This lower variance results in MOCVD being a popular growth technique for industrial scale applications and MOCVD development of high quality spin polarized photocathodes could provide invaluable information if scale up of these devices becomes necessary for future applications [16]. All devices grown for this thesis were grown via Metal Organic Chemical Vapor Deposition (MOCVD) or Metal Organic Vapor Phase Epitaxy (MOVPE). This growth technique is required to allow for high-quality defect-free films to be fabricated. Before discussing MOCVD specifically, additional information about why these epitaxial growth processes are necessary is provided.

2.2 Defects

The primary concern during growth of monocrystalline materials is defect formation. A defect is any imperfection within the crystal lattice. These defects can change both electrical and physical properties of a material significantly. One of the key goals of these epitaxial processes is that, by growing films relatively slowly layer-by-layer, defects of higher dimensionality will not form. Defects can be as minimal as a lack of an atom at a given location in a lattice up to 2 and 3 dimensional defects like grain boundaries and voids. Since epitaxy generally solves these larger scale defects, the primary defects of concern are 1-dimensional defects like threading dislocations.

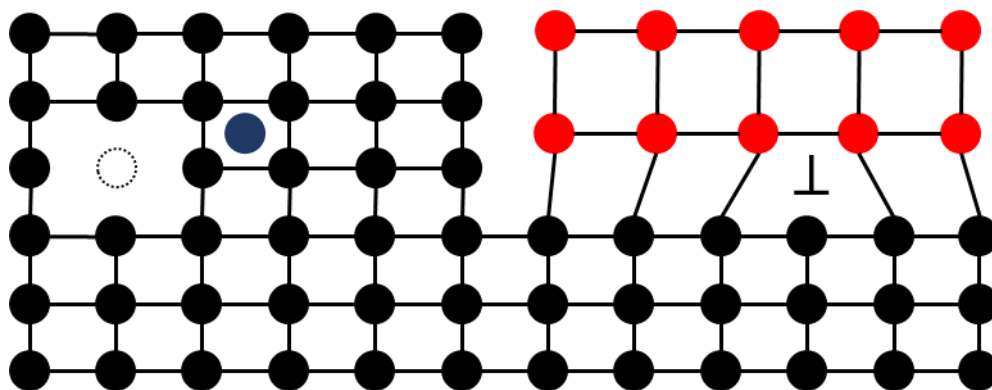


Figure 2.1 Crystal system showing three types of low dimensionality defects: Vacancy (Dashed Circle) Interstitial (Blue Circle) and Threading dislocation (Black to Red)

Figure 2.1 shows 3 common low dimensionality defects. Voids and interstitial defects are known as 0-dimensional or point defects and are generally not as much of a concern as 1-dimensional defects. The primary focus of most high quality epitaxial processes is to minimize the number of thread dislocations formed. Generally, thread dislocations occur when strain is allowed to build up within a crystal structure. After a certain critical thickness, this strain will result in a dangling bond (\perp in Figure 2.1). Thread dislocations occur naturally even during the wafer growth process, but the primary goal is to minimize the formation of and limit those intrinsic defects [17].

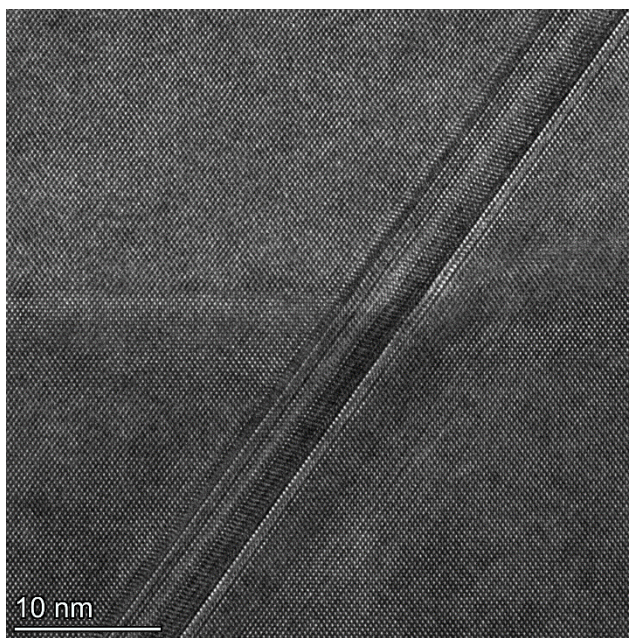


Figure 2.2 TEM image of a misfit linear defect in an MOCVD-grown DBR

Figure 2.2 shows an image taken by transmission electron microscopy (TEM) of a layer with multiple of these misfit dislocations. These dislocations are highly detrimental to device quality for multiple reasons. In traditional optoelectronic devices, these dislocations are the main sites of recombination and, in low dimensionality materials like superlattices, these can cause structural deterioration in the periodicity of the superlattice.

2.3 III-V Background

Most photocathodes are based on materials known as III-V. They are called III-V because the substituent elements of these materials are B, Al, Ga, and In (from the group III of the periodic table) bonded to N, P, As, and Sb (from the group V of the periodic table). III-V materials are the most mature type of compound semiconductor and are used commonly in applications where Si is insufficient. III-V materials are ubiquitous in LEDs and multi-junction ultra-high efficiency solar cells [18].

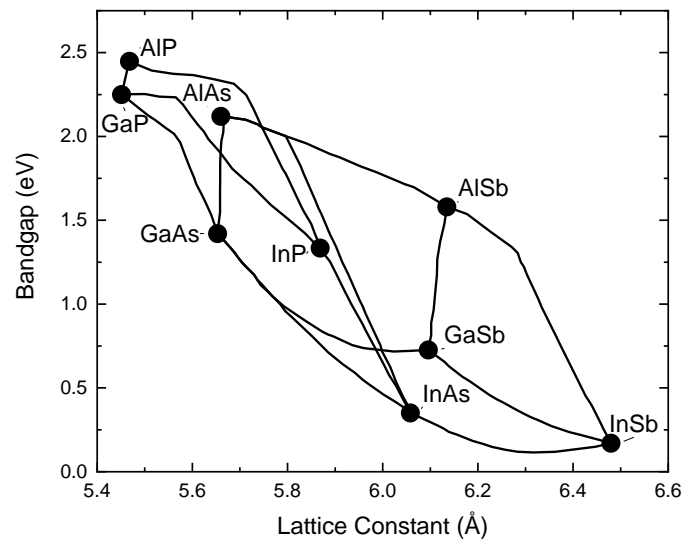


Figure 2.3 Plot of lattice constant vs band gap of all non-nitride III-V semiconductors derived from [18]

III-V materials have unique highly tunable properties (Figure 2.3) making them ideal for a wide array of applications. The tunability of the optoelectronic properties are limited by various manufacturing issues. Compared to many compound semiconductors, III-V materials are extremely sensitive to 1 and 2-dimensional defects. Many of these defects create energy levels located close to the center of the band gap; that means that these materials need to be grown epitaxially to prevent the formation of defects. The chance of defect formation in a material is

dependent on the difference in the lattice constant of the as-grown material and the underlying material substrate. This parameter is known as lattice mismatch [19].

Lattice matching is integral to ensuring high quality films, but in a superlattice photocathode, lattice mismatch is key to obtaining strain. Furthermore, to engineer our intended strain, a compound semiconductor is also necessary. Since III-V alloy substrates are not readily available a new scheme for creating a lattice matched substrate is necessary.

To generate layers with the proper composition and strain, special growth processes need to be done. Known as a pseudomorphic growth, the films' composition, thus their lattice constant, is slowly changed over the films growth thickness. This slow change in the lattice constant allows for the grown film to relax its strain in such a way that defect formation is minimized. The general goal of this processes is to grow a metamorphic layer where the composition varies with thickness. After this layer, a final thick buffer layer is deposited, allowing generally for the resolution of any threading dislocations that form previously. By doing these growths, it is possible to grow a generally defect-free virtual substrate, with a very specific and precise composition, to grow the photocathode on top of.

2.4 MOCVD Growth Process

The two processes used to develop spin polarized photocathodes are molecular beam epitaxy (MBE) and MOCVD. In MBE, the precursor elements are thermally evaporated in a UHV system. Because of the lack of other vapor species, it is possible to grow materials at a high degree of precision. While the precision and quality of MBE are clear, the slow growth speeds and high expense make it difficult to implement these processes outside of a laboratory scale.

In a MOCVD system, chemical precursors are introduced into a reaction chamber. These precursors will then adsorb to the surface and react to form layers. MOCVD can also grow high quality films, but at a much higher rate. Also, since precursors for III-V materials are readily available, various materials can be grown relatively easily in the same system. Instead of vapor pressure and gas-phase precursors, MOCVD utilizes typically liquid precursors. These liquid

precursors are kept at a discrete temperature, and then hydrogen is passed through the precursor. The precursor is then introduced into the growth system via heated lines to the heated substrate. The other precursor is typically a hydride, in our case AsH_3 or PH_3 . Since both of these precursors are gaseous species, they are introduced to the growth chamber via mass flow controllers.



Figure 2.4 MOCVD system used for our growths.

To ensure good epitaxy, the gas flow over the wafer must be a stable, laminar flow, so cascading tiers of MFCs ensure a proper and consistent gas flow rate. While there are multiple configurations for MOCVD systems, the one used in our growths uses a close-coupled shower head structure (Figure 2.4). In this system, the hydride and metalorganic precursors are introduced to the chamber via multiple holes. These holes allow for uniform distribution of the precursors over the film surface. This ensures a uniform composition and thickness across the entire wafer's growth surface.

One special consideration for the MOCVD process is determining the incorporation of gaseous species to the actual grown films. Unlike in MBE systems, where many times elemental or pre-cracked hydrides are used during the growths, in MOCVD cracking occurs within the chamber.

While multiple gas and surface phase reactions can, and do, happen, an idealized reaction pathway for III-V materials is shown below in figure 2.5 [20].

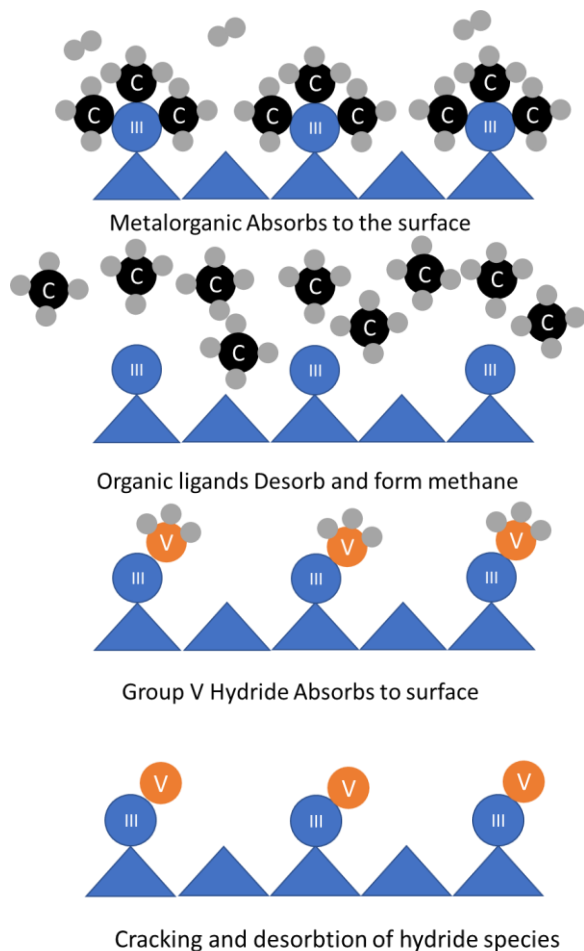


Figure 2.5 Schematic of simplified growth process in MOCVD.

Figure 2.5 shows a generic MOCVD growth process. These processes are strongly governed by kinetics, so ensuring precise gas control is key to having a good, high quality epitaxy. While the above figure provides an adequate general outlook of a MOCVD growth process, examining the key properties of the initial growth surface (substrate) and the overlying layers is important to contextualize various design choices.

2.5. Growth Characterization

Since heteroepitaxy properties can vary significantly with difference growth parameters, processes must be developed to characterize the grown material. Because the characterization of completed photocathode is a time-consuming process, techniques for material characterization, before final device characterization, are key to both ensuring only high quality devices get characterized and provide guidance for subsequent runs. Two types of characterization methods were used to guide growth decision. The first set were in-situ telemetry collected during the growth of the material. The second type were post growth characterization techniques. The in-situ telemetry are key to ensure a high quality growth and, if there is an issue with the growth, it can be seen in real time. The post growth characterization techniques allow for the collection of more information via long acquisition time and destructive characterization techniques.

Before discussing the types of characterization in detail, understanding the layers grown and there necessary parameters is key. A summary of the key characterized layers is summarized below. While the only optically active regions are the surface lattice and the emitting layer, for a high-quality epitaxial growth, all layers must be considered closely. While discussed in more detail in their relevant sections, a brief overview summarizing the key device regions are shown below. To obtain the necessary strain to split the light hole and heavy hole bands in GaAs, the emitting GaAs must be under strain. That means that the superlattice must be grown on a material with a lattice constant smaller than GaAs. The most common material that these strained superlattice is grown on is $\text{GaAs}_{0.65}\text{P}_{0.35}$. Unfortunately, substrates of this specific composition are not commercially available. To overcome this challenge a growth process needs to be devised to grow a high-quality $\text{GaAs}_{0.65}\text{P}_{0.35}$ virtual substrate to grow the strained superlattice on top of. This $\text{GaAs}_{0.65}\text{P}_{0.35}$ must be unstrained and have minimal defects. The process of growing this material is known as a metamorphic growth. In a metamorphic growth process, the composition of the grown layer is changed slightly over the growth surface. This minimizes the formation of defect

formation and allows space for strain to resolve itself. For the developed photocathodes grown here, a step graded metamorphic grading was developed. In a step-graded process the composition is changed after a given growth thickness. The composition then remains constant for a given thickness, then a new composition layer is grown on top of it [21].

Engineering the strain in this metamorphic grading is key because it ensures that the GaAs superlattice is properly strained. It is also critical because films grown with a high degree of strain have less uniform lattice planes. This results in rougher surfaces (poorer photoemission) and worse superlattice fidelity.

The other layer of key importance is the superlattice. The superlattice is the layer that actually photoemits the spin polarized electrons, so ensuring a high quality superlattice is particularly important. Because the layers within the superlattice are on the scale of nanometers, ensuring a high fidelity in the layer (lack of Phosphorous intermixing) is key to achieving a high degree of polarization. Ensuring a high degree of periodicity is also key because, if layer thicknesses are nonuniform, strain relaxation will occur thus lowering the peak polarization.

Ensuring a high quality epitaxy requires continuous monitoring of the growth process. Films can be characterized in two ways: during the process (in-situ) and after final film growth (ex-situ). While in-situ processes typically cannot glean as much information as ex-situ ones, they are invaluable because they provide information about the qualities and properties of the films developed during the growth itself.

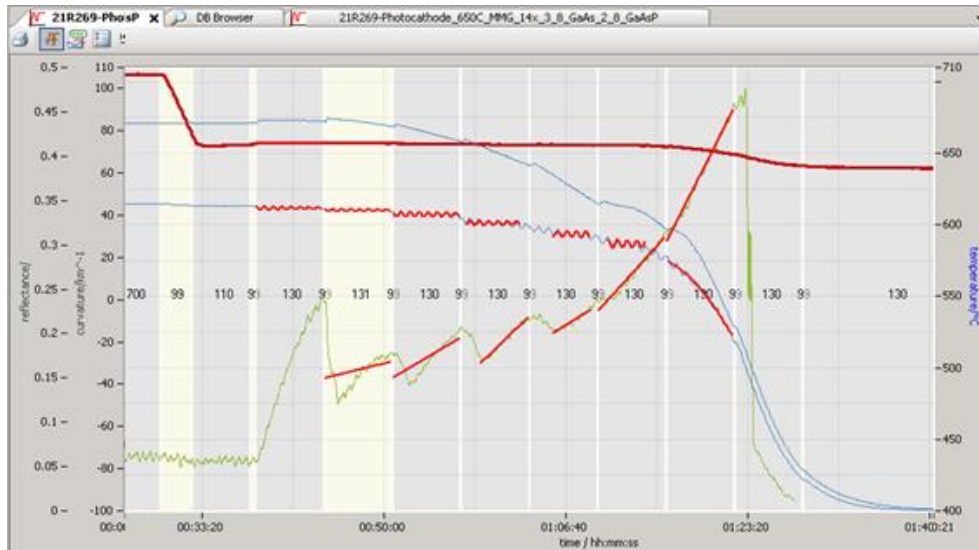


Figure 2.6 Example of growth Telemetry for an MOCVD process. The plot shows Temperature (Red), Reflectivity (Blue) and Curvature (Green)

Figure 2.6 shows an example of in-situ measurement telemetry for one of our MOCVD processes. There are 3 discrete measurements done: pyrometry, curvature and reflectivity. Using these 3 measurements in confluence, important information about the growth process can be determined. This is especially true for curvature and reflectivity measurements because, if these properties deteriorate during the growth, fault finding and modification in the growth process can be made.

2.5.1 Pyrometry

The kinetics-based growth mechanisms of MOCVD make precise temperature control integral to ensuring target film quality and composition [22]. Many growth systems have thermocouple temperature systems integrated into them. While these thermocouples can provide important insight, they do not give temperature data of the main region of concern: the growth surface. In order to measure the temperature of the growth surface, a non-contact method with a high degree of precision at expected growth temperatures is necessary. To achieve this, emissivity-corrected pyrometry is used. Pyrometry is the process of measuring the emitted radiation of a surface based on temperature, following the formula:

$$I = \epsilon\sigma T^4 \quad (2)$$

where I is the radiant heat power emitted from a surface, σ is Boltzmann's constant, T is the temperature and ϵ is the emissivity of said material. This relation (Stefan-Boltzmann Law) relates the intensity of emitted radiation to the temperature of the material measured. Emissivity can be thought of as the efficiency at which a material can emit light and is both material and temperature dependent. Properly calibrating emissivity for a given growth temperature and material is key to ensuring an accurate temperature reading.

2.5.2 Curvature

Especially when growing non-lattice-matched materials, the surface grown will be strained. To monitor the evolution of the strain within a material during the growth process, specialized curvature measurements are done to analyze the properties of strain within the film [23].

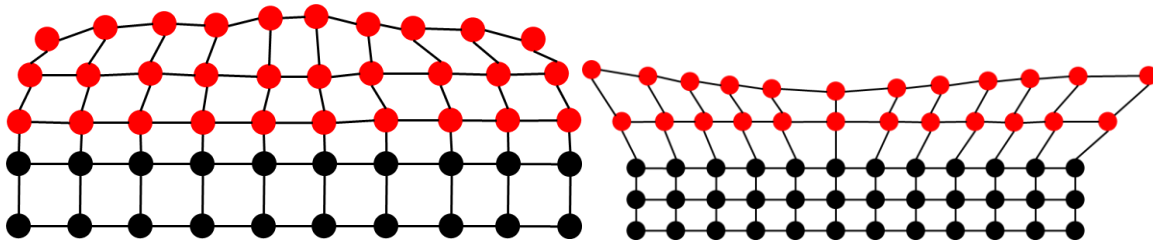


Figure 2.7 Example of how lattice mismatch of grown film and substrate can create curvature (highly exaggerate for demonstration purposes).

Depending on if the strain is tensile or compressive (Figure 2.7), the growth surface will bend in a given direction. This can be quantified by using two lasers a known distance from each other. The lasers will reflect from the sample surface and the difference between the distance of the incident laser and the reflected laser are measured. If the surface is concave, the distance between the lasers will be closer to each other. Conversely, if the surface is convex, the distance between the reflected lasers will be further away.

2.5.3 Surface reflectivity

While curvature measurement is implicitly a reflectivity measurement, it is not a reflectivity measurement. Reflectivity can give two distinct properties of a growing film. First by measuring surface reflectivity, the general quality of the epitaxy can be inferred. Generally, the smoother the surface, the higher the quality the epitaxy will be. Examining the reflectivity of a surface is key because curvature measurements are highly dependent on surface quality. Examining Figure 2.6, near the end of the growth, there is a significant increase in curvature, but there is also a significant decrease in reflectivity. Since curvature is dependent on reflectivity, curvature measurements on highly rough surfaces are not necessarily accurate.

When surface reflectivity measurements are performed, two different wavelengths are used. One wavelength is at 450 nm (3 eV). At this higher wavelength, the reflected laser is surface sensitive due to absorption of the incident light. The other wavelength is 951 nm (1.3 eV). At this wavelength, absorption is significantly lower, so the reflectivity measurement can probe deeper into the film. This can cause oscillations in the reflectivity measurements. These oscillations, or interference fringes, are a secondary way to measure growth rate. This is done by measuring the periodicity of the interference fringes.

2.6. Post Growth Characterization

While in-situ measurements are integral for observing the quality of a film during growth, they have some distinct limitations. The key limitation for these in-situ processes is that they cannot interact with the growth process. This limits the techniques that can be used to non-contact measurements with relatively short acquisition times. To obtain more meaningful information about a growth process, multiple post growth ex-situ characterization techniques can be performed. These characterizations can be both destructive and nondestructive in nature, and are the primary way that the initial growths are characterized.

Outside of the in-situ telemetry used to monitor growth conditions, multiple other characterizations were used to ensure the quality of the grown devices. The two most common characterization

techniques used were Nomarski Microscopy and High-Resolution X-Ray Diffraction (HRXRD). Nomarski was used as a powerful preliminary qualitative analysis technique to determine general film quality, and HRXRD was the primary tool used to determine relaxation within the grown layers. Additionally, Transmission Electron Microscopy (TEM) and spectroscopic ellipsometry were used to examine the quality of the final superlattice and extract optical properties, respectively. Final Device testing was done using a micro Mott polarimeter.

2.6.1 Nomarski Microscopy

While ex-situ processes can be destructive and highly qualitative, rapid quantitative measurements can provide a significant amount of information. One of the most common of these techniques used is Nomarski Microscopy. Nomarski microscopy is a type of differential interference contrast (DIC) microscopy. Nomarski is unique because it uses two beams of light to measure an image. These two beams originate from the same polarized light source. The reflected beams are then analyzed with another polarizer to generate an image. This methodology of generating image allows for the observation of much smaller feature sizes than traditional reflective microscopy [24].

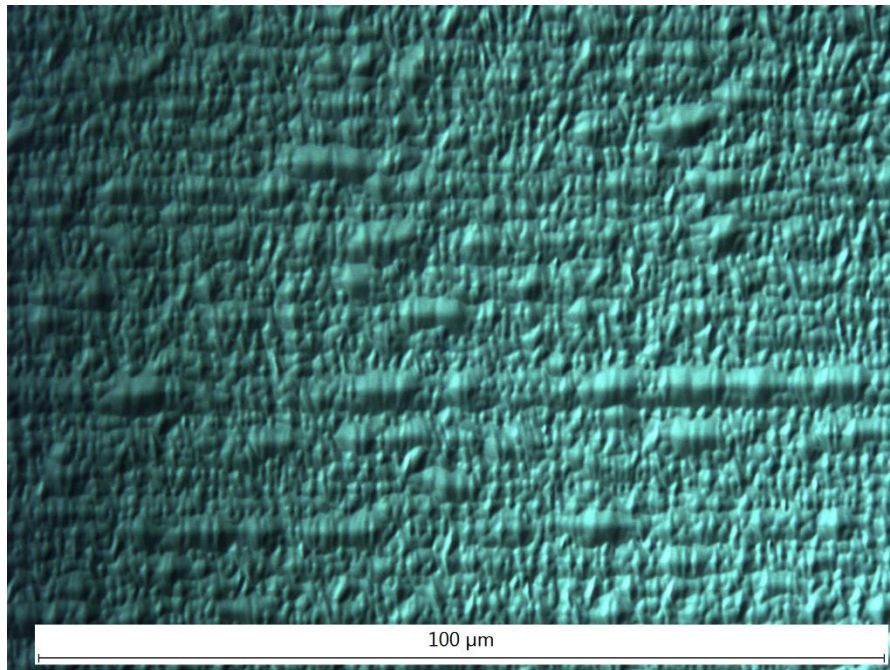


Figure 2.8 Example of Nomarski Microscopy image of metamorphic grading

Nomarski microscopy is key to understanding the surface topography of grown samples. As Figure 2.8 shows, Nomarski microscopy has a high degree of fidelity even at extremely high magnifications. This can be reached without modifying the surface.

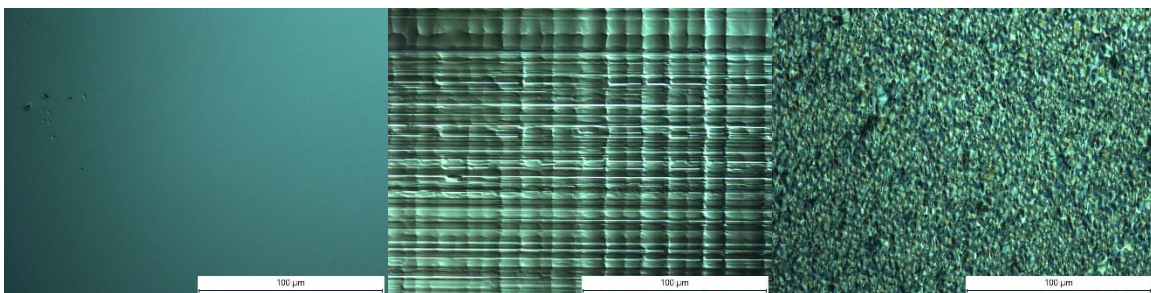


Figure 2.9 Nomarski of layers with 3 different qualities of epitaxy. Left: GaAs_{0.95}P_{0.05} minimal strain in the grown layers so minimal surface features; Middle: Textured photocathode; Right: poorly relaxed growth.

For epitaxy, the “smoothness” of the final growth surface and the periodic facets along the surface can give insight to the quality of the epitaxial process. Figure 2.9 shows three different MOCVD growths with their resultant surface quality. The left most figure shows GaAs_{0.95}P_{0.05} on GaAs. There is only minimal lattice mismatch between the two, and this results in a surface with minimal

features. The middle figure shows a completed photocathode surface. Within this system, there is a significant lattice mismatch between the layers and the substrate, but, due to the precise control of strain relaxation, the surface is smooth with specific faceting trenches. For the rightmost image, the strain was not resolved well, and a periodic nature was not observed.

2.6.2 X-Ray Diffraction

High Resolution X-ray Diffraction is a key tool for quantifying epitaxial materials; since our goal is to grow a relaxed metamorphic grading with a strained superlattice on top, HRXRD is a key technique for measuring material strain and composition.

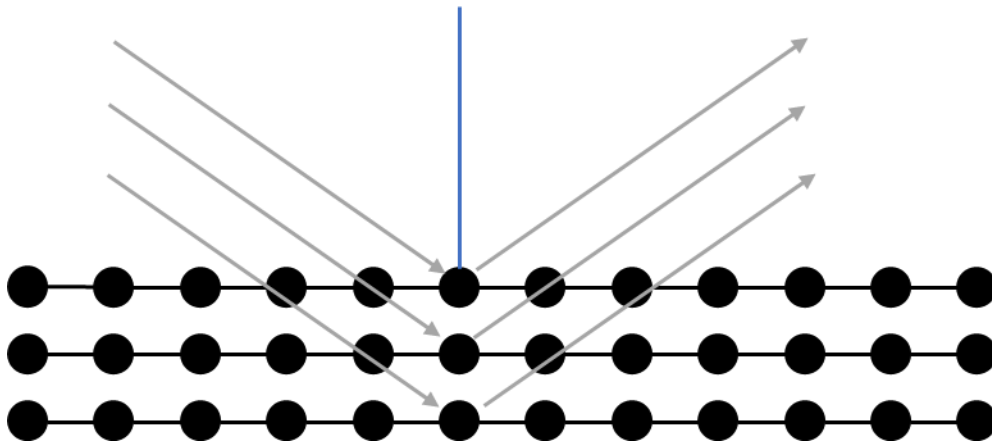


Figure 2.10 Basic Example of the Bragg condition

X-Ray Diffraction works by analyzing the destructive and constructive interference that occurs when an X-ray impinges on the sample (Figure 2.10). The most fundamental equation for X-ray diffraction is known as the Bragg Condition:

$$\lambda = 2d_{hkl}\sin(\theta)$$

(3)

where λ is the wavelength of the incident X-ray (source dependent), d is the interplanar spacing (the distance between atomic planes, within a structure) and θ is the angle at which the Bragg condition is satisfied. Typically, when an X-ray is directed at the surface, destructive interference

will occur and no peak can be observed. When the Bragg condition is satisfied, a peak will be observed.

While basic detector and sample rotations are useful for polycrystalline or powder samples, to extract meaningful information out of high-quality monocrystalline samples, even more specialized X-ray techniques have been developed. Two different X-ray diffraction techniques were utilized to characterize grown samples: coupled rocking curves and reciprocal space mapping.

A coupled scan is a special type of X-ray diffraction scan that couples two other basic scans: rocking curves and detector scan. By changing the angle of the sample and the detector angle simultaneously, the diffraction vector (the blue line in Figure 2.10) will remain constant. This type of scan is key for examining properties of the grown superlattice. These coupled scans allow for information to be extracted about composition, layer thickness, and the periodicity of the superlattice. These coupled scans are also key because they are the fundamental measurement technique used to examine the strain and relaxation within the metamorphic grading: reciprocal space mapping [26].

Crystalline structures can be thought of as a highly periodic structure, where the intensity of the reflection is the relative number of those interplanar spacing. Instead of treating these interplanar spacings as a known distance, we can do a dimensional transform to treat a known interplanar spacing as a discrete point. Then, by varying the scanning condition, it is possible to map how those interplanar spacings change within a growth system. Examining how these interplanar spacings change, and the underlying mechanism of how they change, is one of the key goals of reciprocal space mapping. Fundamentally, reciprocal space mapping takes a series of coupled scans discussed previously to examine how interplanar spacings change.

One of the major limitations of a traditional coupled scan is that they are typically done normal to the surface. When performed normal to the surface, the difference in interplanar

distance can be observed, but examining why it is changing can be nontrivial. For our purposes, the interplanar spacing can be changed via two discrete systems: strain and composition. Via strain, the lattice constant will be fundamentally different because of different bond lengths. When the composition of the grown layer is changed, the system can sometimes remain relaxed, but more often the lattice constant will fundamentally change because the material itself changed. While this can be observed to some extent by rotating the sample and doing multiple symmetric reciprocal space maps, an asymmetric scan will be able to examine both simultaneously.

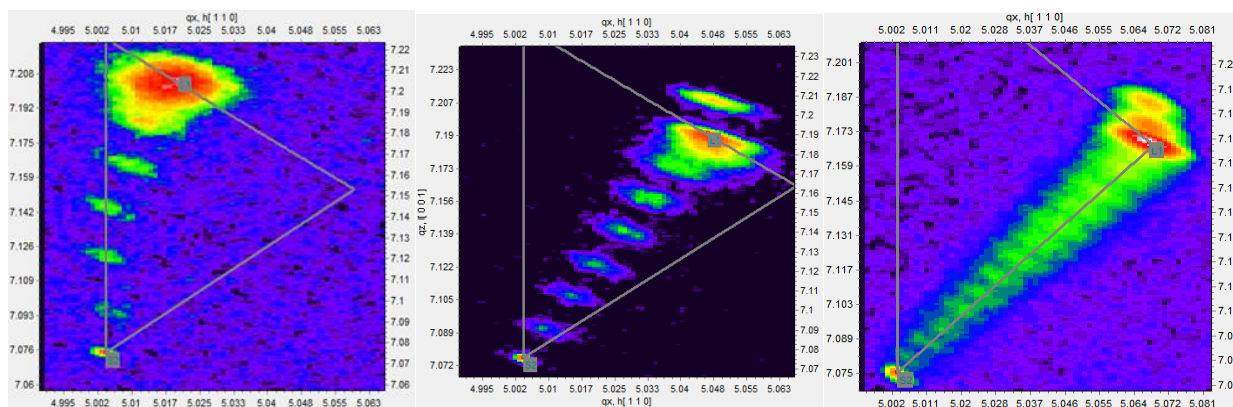


Figure 2.11 Three different reciprocal space maps showing metamorphic grades of 3 different strains.

Figure 2.11 shows three different asymmetrical reciprocal space maps. Going from left to right, the films go from being fully strained to completely relaxed. Based on the location of the reciprocal lattice points (the bright points in the map) and their relative location within the strain triangle, a significant amount of information can be extracted about the growth quality of a given metamorphic grade. Observing and analyzing these reciprocal space maps was the key way in which the metamorphic grading itself was characterized [27].

2.6.3 Spectroscopic Ellipsometry

While testing the electron emission of the photocathodes is important, a secondary way to confirm both composition and quality of the deposited films is via spectroscopic ellipsometry. Using spectroscopic ellipsometry, it is possible to examine the optical transitions within the film and

determine the overall thickness of the layers. The underlying principle of ellipsometry is simple. When light interacts with a media, it can either reflect or transmit. When the light travels through said media, the propagation of the light will change. the change in how light propagates through various media, can then be quantified by analyzing the difference in polarization between the incident light and the reflected light. The real form components of the electric field, describing how a plane wave propagates through a medium, are given by:

$$E_x = a \cos(\omega t - \beta z + \phi_a) \quad (4)$$

$$E_y = b \cos(\omega t - \beta z + \phi_b) \quad (5)$$

where E_x and E_y are the components of the electric field, a and b are the amplitudes of the respective component, ω is the angular frequency, β is the propagation constant, and ϕ is the phase angle. Ellipsometry works by quantifying how the polarization of light changes based on how ϕ (phase) changes due to how the light propagates through a medium. This is because β is both material and frequency dependent [29] and is given by:

$$\beta = \sqrt{\omega^2 \mu \epsilon} \quad (6)$$

where ω is the frequency of the electromagnetic wave, μ is the magnetic permeability, and ϵ is the dielectric permittivity. Since ellipsometry is dependent on the transmission and reflection through various materials, the change in propagation constant through the sample media will result in a change in ϕ in the outgoing light, thus the polarization will change. Since how light interacts with media is dependent on both wavelength and angle of incidence, multiple wavelengths and angles of incidence are typically analyzed.

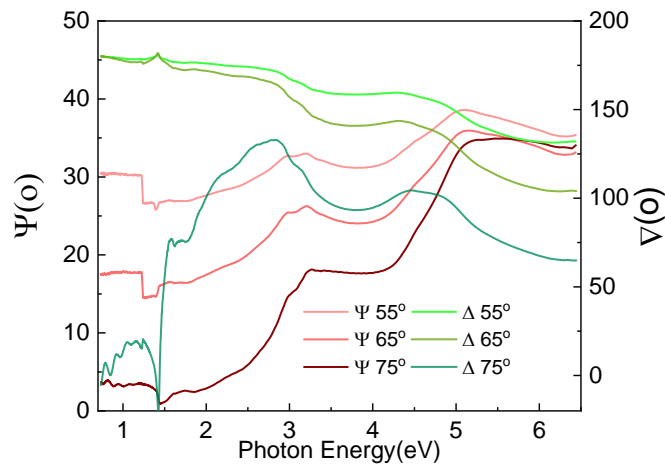


Figure 2.12 Example of raw ellipsometry data measured on a GaAs wafer.

Figure 2.12 shows an example of ellipsometry measurement. The changes in polarization are represented via Ψ and Δ using the following equation:

$$\tan(\Psi) e^{i\Delta} = \frac{\tilde{r}_p}{\tilde{r}_s} \quad (7)$$

Where \tilde{r}_p is the Fresnel coefficient for the parallel plane of incidence, \tilde{r}_s is the Fresnel reflection coefficient perpendicular to the incident plane, $\tan(\Psi)$ is the amplitude ratio between the two reflections and $e^{i\Delta}$ is the phase difference [29].

While these parameters provide an accurate representation of the measurement, they are not directly meaningful. To obtain useful information from these ellipsometry measurement, the data is modeled until minimal error can be observed between the measured data and the modeled data. There are two generally accepted ways that ellipsometry can be measured: empirical and oscillatory. In an empirical model, the measured film is treated as either a transparent or absorbing film, then using a B-spline model (for absorbing) or a Cauchy model (for transparent), the data is modeled. While these empirical models can provide significant insight into the properties of a film, an oscillatory fit model can provide much more insight into the optical properties. An oscillatory

model works by modeling the discrete optical transitions within a material. Using such a methodology, the underlying optical transitions within the material can be extracted.

2.6.4 Transmission Electron Microscopy

All the previously discussed measurements are non-contact measurement techniques. Transmission electron microscopy (TEM) is an invaluable tool for characterizing small-feature films down to the atomic scale. TEM works by focusing an electron beam to an extremely fine point. This beam transmits through the sample and various data can be obtained. For the context of this thesis, 3 different measurements were used: TEM micrographs (Images), Selected Area Electron Diffraction (SAED), and Energy Dispersive X-Ray Spectroscopy (EDS). Because the electrons need to transmit through the sample, special sample preparation must be done. The resulting lamellar needs to be <100 nm. Multiple techniques have been developed to prepare the samples. While techniques like sample grinding and ion milling can be used, the most desired technique for TEM sample preparation is through focused ion beam (FIB). This is because of the high degree of precision that FIB has over other sample preparation techniques.

A TEM micrograph is simply the image extracted by the TEM. There are multiple techniques used to obtain an image via TEM. These techniques can be split, in our context, into categories depending on the detector scheme and what property of the beam is being examined. All images were taken using a High-angle annular dark-field imaging (HAADF). Dark field images are images generated without using data from the incident electron beam. The image is generated by scattered electrons and not by the directly transmitted beam itself. This allows for a higher z-contrast within the images. The high-angle annular refers to the detection scheme of the detected electrons. By using a high-angle annular field, it is possible to examine electrons scattered and, since the extent of the scattering is dependent on the size of the scattering item, a significant amount of z-contrast is available in heavy atoms [30].

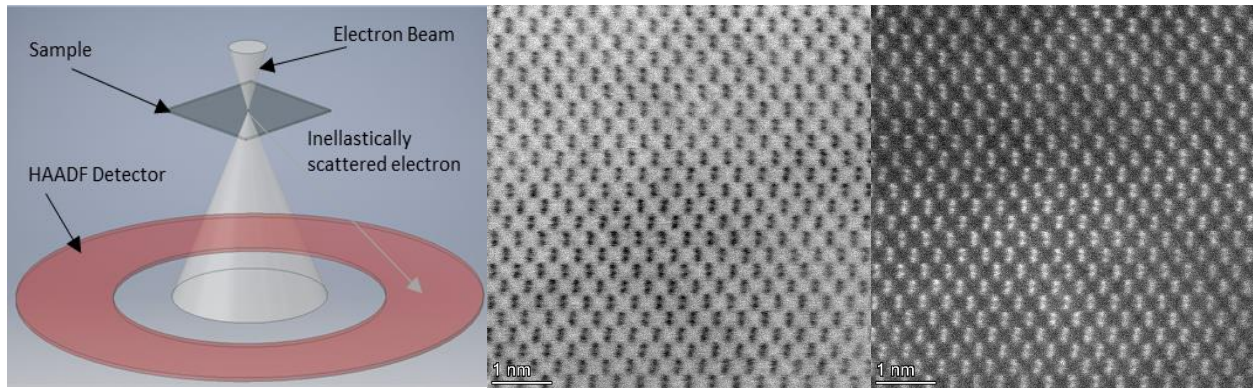


Figure 2.13 The Detector Scheme for a HAADF (derived from [30]) system alongside Two HAADF images showing atomic-scale Resolution

Figure 2.13 shows a HAADF detector scheme and multiple HAADF images. By examining the integrated intensity within the annulus for a given probe position, an image is generated. As Figure 2.13 shows, atomic resolution can be obtained with a high degree of precision using HAADF detector. As the figure also shows, often the images are shown in a bright field mode and an optical transform is done to reverse the image to improve visual clarity of the micrograph.

TEM can generate more than just simple micrographs. As shown with HAADF detection scheme, the image is taken by examining the integrated intensity of electrons impinging on the annular detection area. The nature of the diffraction itself can also be examined. One of the unique properties of TEM diffraction is how localized it can be. For HRXRD, the X-Ray beam could have spot size in the range of mm. This means that the irregularities within the observed area will be averaged in. With a TEM, the area of diffraction can be selected specifically to observe the diffraction in that region (Figure 2.14).

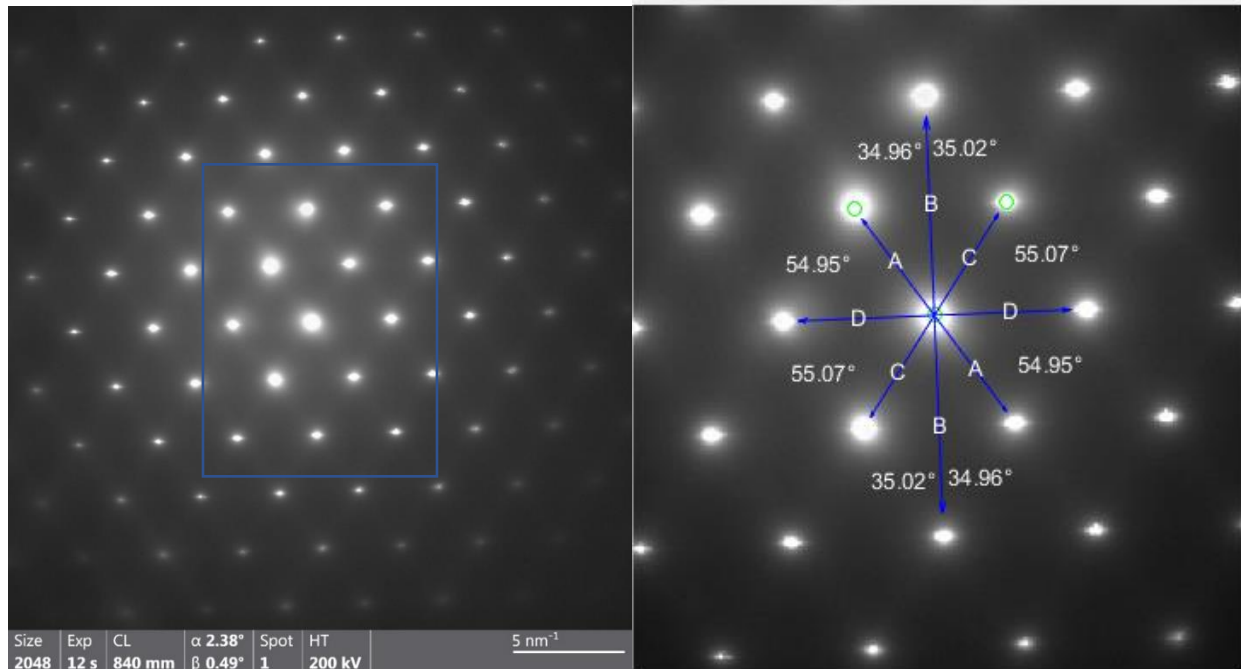


Figure 2.14 Example of diffraction pattern and analysis for one of our samples along with a sample showing the reciprocal space vectors

Like reciprocal space mapping, the results of SAED is in reciprocal space. Each point corresponds to a given lattice plane. By examining these distances two things can be found. First, the presence of multiple lattice points at a given distance shows the presence of multiple grains within the diffraction area. Second, by extracting the interplanar distance, things like lattice constant and crystal structure can be calculated to a high degree of precision.

The final technique done in confluence with TEM is Energy Dispersive X-Ray Spectroscopy. EDS is unique in TEM because it mitigates one of the key problems with SEM EDS: excitation volume. Typically, the excitation volume for EDS is on the scale of 1-2 microns into the film. This means for standard Scanning electron microscopy (SEM), compositional mapping is not meaningful in a lot of cases. Because TEM samples are less than 100 nm thick, the excitation volume is then limited by the actual thickness of the sample instead of the potential excitation volume of the electron beam. This can be exploited to obtain high resolution compositional mapping of samples (Figure 2.15).

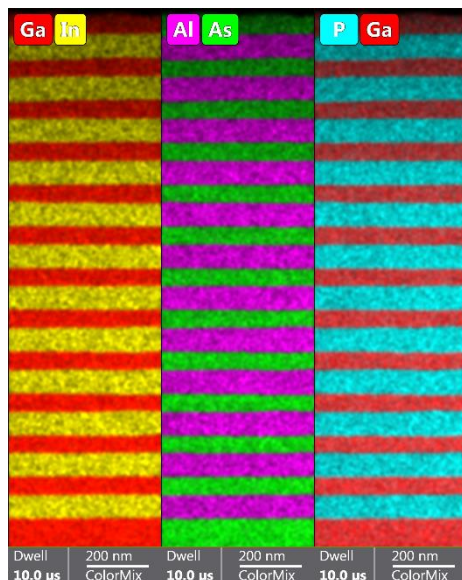


Figure 2.15 Example of EDS mapping of the various elements within the DBR

By using these 3 TEM measurements in confluence, key information can be discerned. First, by looking at the micrograph, the general quality of the superlattice fidelity can be extracted. SAED can then be used to see if the superlattice structure is correctly strained. Since, the GaAsP is relaxed and the GaAs is strained, only 1 set of reciprocal points should be present for a given plane. Finally EDS mapping can be used as a technique to both verify fidelity of the superlattice and examine loss of fidelity in more detail. Because of the thickness of the grown metamorphic grading, TEM measurements were limited to the superlattice. This is the key area of interest from a device perspective because it is the only area responsible for photoemission.

2.6.5 Atomic Force Microscopy

Obtaining a high quality surface is key to a high degree of polarization. This is because the incident photons hitting the surface are circularly polarized and, if the surface is highly nonuniform, scattering could change the polarization of the incident laser light. While preliminary Nomarsky measurements give insight into the macroscopic surface structure, certain features are below the observable limit of Nomarsky microscopy. To observe these microscopic/nanoscale features, atomic force microscopy (AFM) was used. In AFM, a fine needle comes in contact with the surface

of the sample. The surface is then mapped as the needle moves across the surface. As the needle moves across the surface, a topographic map will be created. This topographic map provides significant information of the uniformity across the surface. By examining the surface topography information about the quality of the growth can be discerned. Examining growth properties is key to improving surface quality thus minimizing surface depolarization effects.

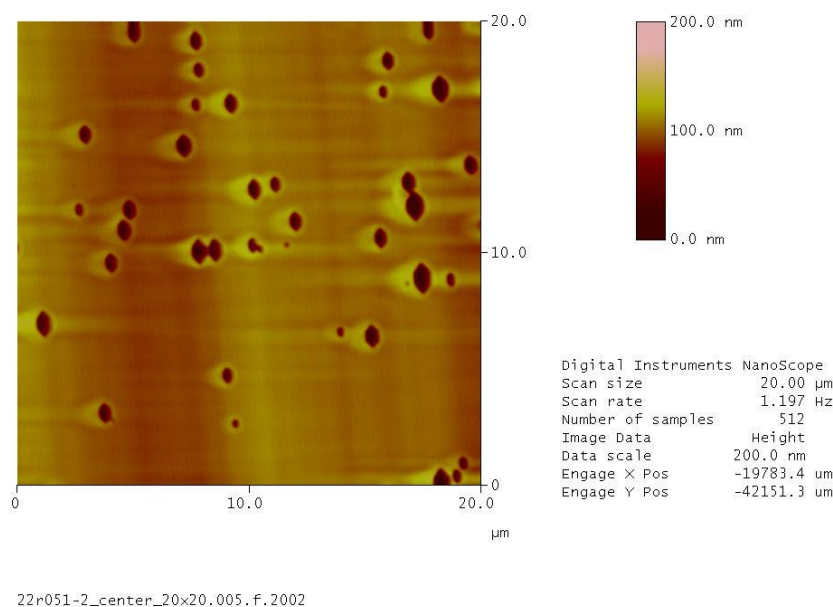


Figure 2.16 Example of an AFM image on one of our samples

Figure 2.16 shows an example of AFM on a completed photocathode. As the AFM shows, the general surface is relatively smooth, with localized surface irregularities. One way to observe the overall quality of a completed device is to examine the density and severity of these surface irregularities.

2.6.6 Hall Effect

Since the entire structure is p-type, and target doping of certain regions is key, having a way to quantify doping is important. The challenge of doping is complicated by the nature of our growths. The primary doping agent for the majority of the structure is diethyl zinc. However, diethyl zinc

incorporation into the film is highly temperature dependent. Since some of our growths exceed 700°C, ensuring the proper doping level is key [31]. Hall effect works by measuring the change in electric field in a sample when a voltage is applied across it in a magnetic field. Because a current is running through the sample, to obtain an accurate doping concentration, the thickness has to be known [32]. Since Hall effect measurements are done on the entire structure, if there are layers of varying carrier concentration, the extracted concentration could be a weighted average of the carrier concentration of the entire stack. For this reason, hall effect measurements were done on samples which were grown on undoped GaAs wafers.

2.6.7 Device Testing

All the previous characterization techniques are integral to analyze the quality and properties of the deposited layers. While these characterizations are key to growing a high quality material, the final goal of this process is to create a device that will photoemit spin polarized electrons. Creating a system that can generate and measure spin polarized electrons is non-trivial, and specialized and precise instrumentation is necessary.

These measurements were performed at the Thomas Jefferson National Laboratory in Newport News, Virginia (JLab) and at the Brookhaven National Laboratory in Upton, New York (BNL). A summary of the physics behind the measurements and of the instrumentation itself is summarized below. All the included pictures are from JLab, but the process of measurement and characterization are the same at BNL.

The system used to generate and measure spin polarized electrons is known as a Mott Polarimeter. A Mott Polarimeter must do 4 things: activate the photocathode, generate spin polarized electrons, direct them to the detection system, and measure the directed electrons.

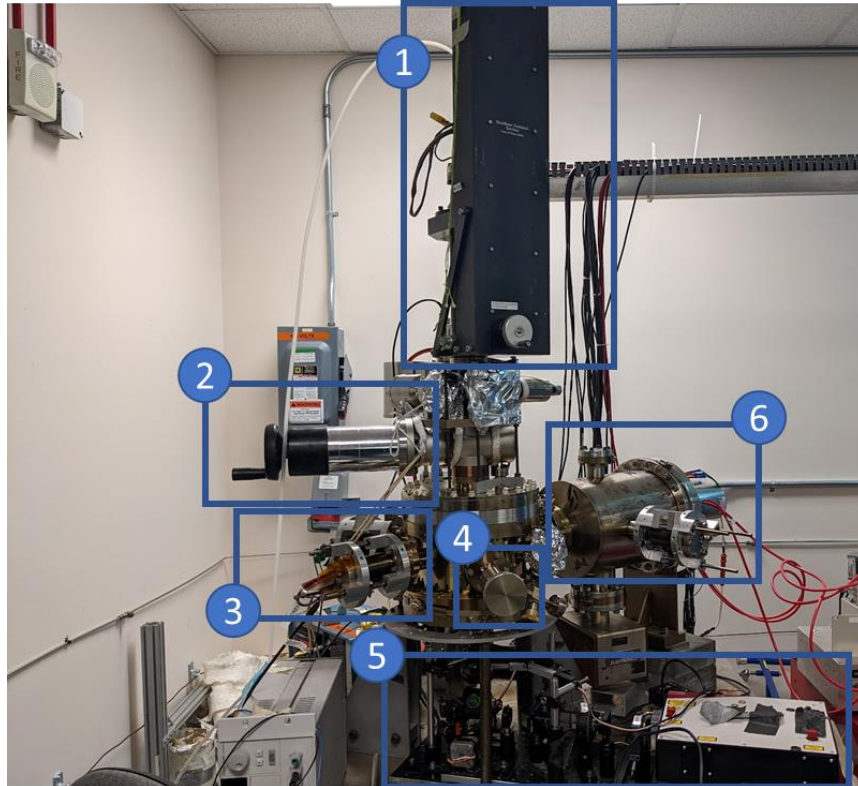


Figure 2.17 The Mott Polarimeter 1: the mounting Stalk 2: UHV Isolation Valve 3: Cesium heat source 4: NF3 leak valve 5: Laser Optics 6: Mott Polarimeter

Figure 2.17 is an image of the Mott Polarimeter at JLab. Each of the highlighted regions is key to obtaining high quality measurements. To introduce the photocathode to the system, it is mounted onto a Molybdenum stalk. A piece of indium foil is placed between the sample and the molybdenum stalk. During heat treatment, the indium will melt and make a high-quality thermal/electrical contact.



Figure 2.18 Photocathode mounted on the molybdenum stalk with the tantalum press contact.

The photocathode is then held in place by a tantalum press contact. Because of the UHV nature of these measurements, low outgassing materials are necessary, hence the molybdenum and tantalum. The testing chamber is kept at UHV condition by 3 ion pumps. Two of these ion pumps are mounted on the main chamber, and the third is in the Mott portion of the chamber (label 6 in Figure 2.17).

After being mounted the sample can then be introduced into the chamber using a standard load-lock system. The device activation process can begin. Initially, the photocathodes will not be able to emit electrons. This is because negative electron affinity surface treatments must be performed. The first step for a fresh photocathode is heat cleaning. During this process, the photocathode is heated in UHV to remove any surface contaminants. This step also melts the indium foil behind the photocathode creating a high quality thermal/electrical contact. After heat treatment, the actual activation process can begin. The goal of this first activation process is to create the negative electron affinity surface to facilitate easy photoemission, so the exciting light energy and polarization do not necessarily matter.

For the activation process, both cesium and NF_3 are used. While oxygen is a commonly used oxidizing agent, NF_3 creates a stronger surface dipole thus facilitating more photoemission [33]. Cesium is introduced into the system using a specialized cesium alloy. When this alloy is heated with a nichrome wire, it preferentially evaporates cesium. The NF_3 is introduced via a leak valve. During the activation process, the photocathode is kept at a voltage of -300V and the photocurrent is measured by examining the current between the photocathode and the ground. Electrons that come in contact with a portion of the chamber will generate a current loop and that current is measured.

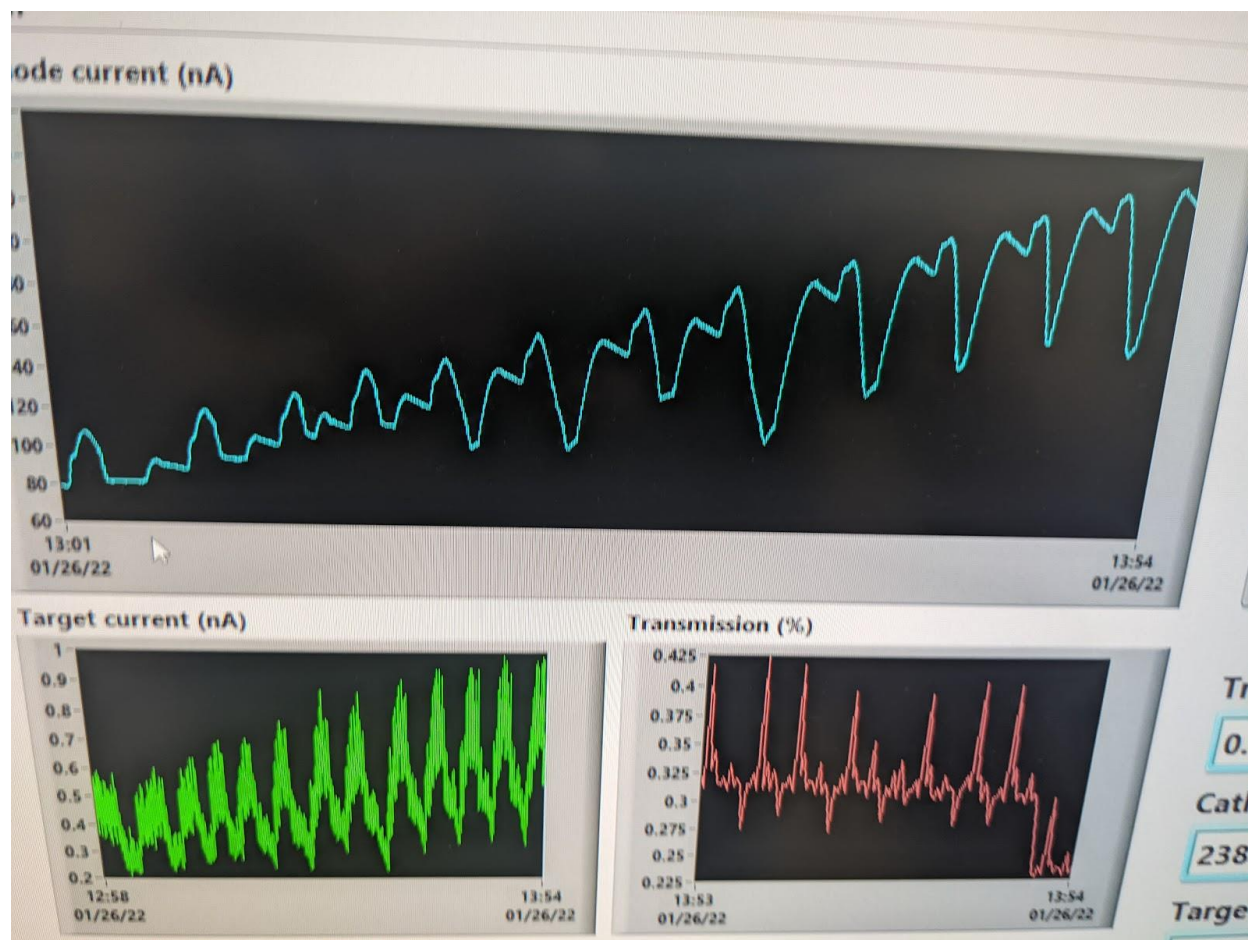


Figure 2.19 Image illustrating the activation process (Anode current, target current and transmission)

The blue curve in Figure 2.19 shows the photocurrent during activation process. Depending on the flux of Cs and NF_3 , the current changes. During the cesium introduction, there is a common

inflection point that consistently occurs in the current measurement. That is because the instrumentation setup cannot differentiate between the Cs ion current and the photoemission current. Once the cesium is turned off that excess current is removed. The activation process is usually referred to as a yo-yo process, because the current varies higher or lower during the deposition process. One “yo-yo” cycle is as follows:

1. Cesium is introduced, photocurrent is increased (one initial peak will be seen due to the initial ion flux of Cesium, but that peak should be constant for each cycle)
2. Excess cesium initially causes an increase in photocurrent, but as the amount of cesium increases the dipole weakens and current drops.
3. Cesium is shut off
4. NF_3 is introduced into the chamber, a stronger surface dipole forms and electron current increases
5. Photocurrent plateaus. NF_3 valve closed

The above process is repeated until there is negligible change between the current with the two activation cycles.

After activation, the electron current must be directed to the Mott polarimeter. This is done in two steps: aligning the electron beam using electrostatic lenses and finding the optimal transmission point on the surface of the photocathode.

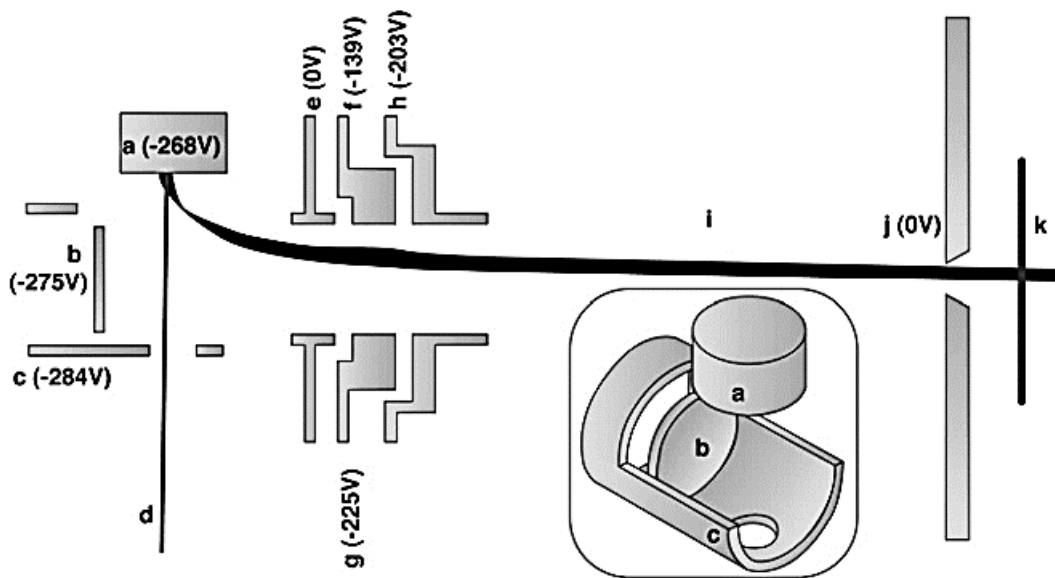


Figure 2.20 Illustration of the electron optics used to direct the electron beam to the Mott derived from [33].

As shown Figure 2.20, laser light comes in through d, then the first set of lenses (a, b and c) deflect the photoemission beam to the Mott lenses (e, f and h). These set of lenses are key to initial Mott calibration. While the potential of these electrical static lenses are not necessarily relevant to the electron current during activation, careful steering of the electron beam using these sets of lenses is key to actually obtaining a sufficient electron current to the Mott. To obtain this current, the electrostatic potential of these lenses are changed and the response of the target current (the green line in Figure 2.19) is examined. The potential of these lenses are varied until the target current reaches a maximum value.

One of the key challenges with obtaining a sufficient target current is that the transmission of electrons from the photocathode to the Mott polarimeter is not uniform spatially across the photocathode surface. For that reason, transmission mapping must be performed.

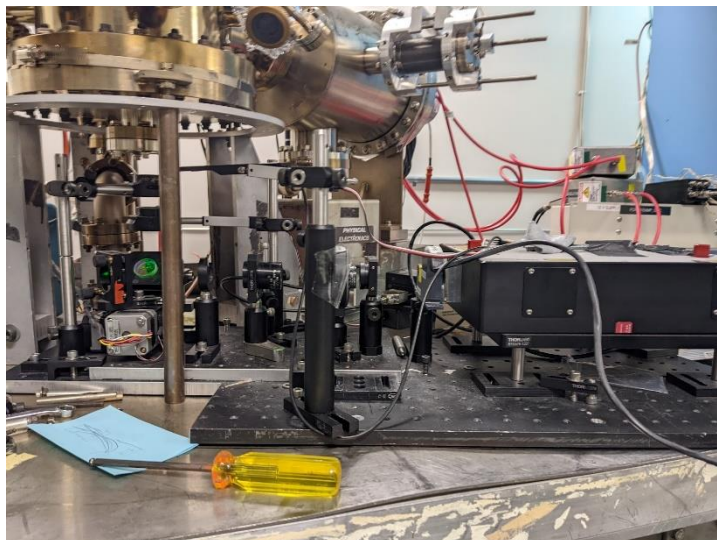


Figure 2.21 Image of tunable white light laser with polarizing and filtering optics

During the transmission mapping process, the exciting laser for the photocathode is moved across the surface of the photocathode via a set of servo motors (Figure 2.21). The photoemission and the transmission to the target is then mapped, and the location of maximum transmission is then found. After this point is found, final finetuning of the lenses can be performed to further maximize transmission to the Mott.

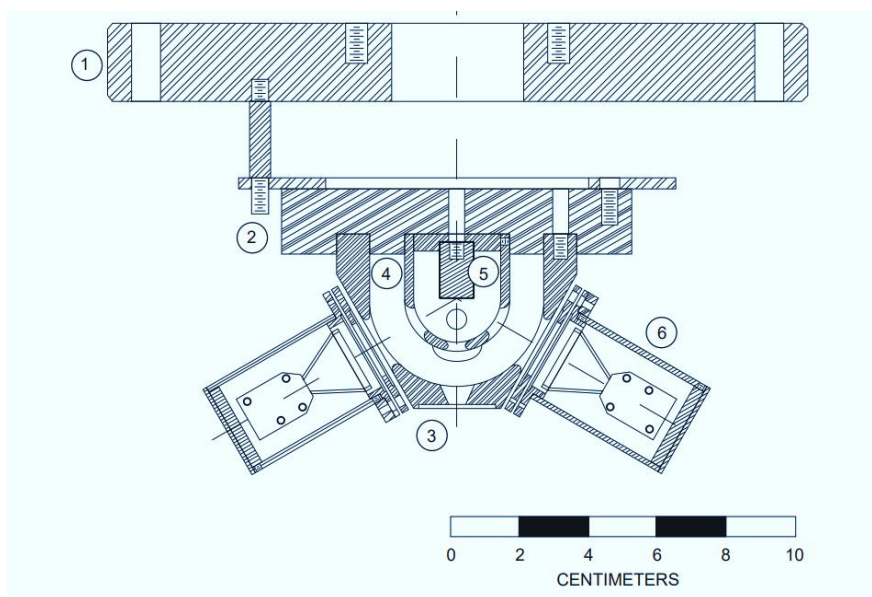


Figure 2.22 Schematic of the Mott Polarimeter derived from [33].

The full process for polarization measurements can be found here [33] but a brief overview of how the process works is outlined below. The spin polarization of the electron beam is measured using a piece of instrumentation called a Mott polarimeter. In a Mott Polarimeter, the photoemitted electron beam is accelerated into a gold coated target. Via coulombic interactions, electrons of a given spin will preferentially scatter in a given direction. As these electrons scatter, they will decelerate through an electric field until, finally, they reach a rejection mesh. This mesh steps through various voltages and rejects electrons based on their energy. Behind this mesh, is a channel electron multiplier which counts the number of electrons that make it through this mesh. By examining the number of elastically scattered electrons, and comparing the two different electron multiplier counts, the asymmetry or spin polarization can be measured. Via coulombic interactions observed in Rutherford scattering, electrons of a given spin will scatter in a different direction. To calculate the extent of polarization the asymmetry between the two channel multipliers is analyzed along with the Sherman Function. The Sherman Function is the probability of an electron of a given spin to diffract at a given angle. In most cases, the Sherman Function is an instrumental parameter dependent on the angle of the two channel electron multipliers.

Chapter 3: Composition Calibrations and Metamorphic Grading Optimization

3.1. Introduction

Group III-V materials are inherently vulnerable to defects within their lattice. This is because the defects within GaAs create energy levels that are close to the middle of the band gap. This results in a higher recombination rate for these traps. One way to mitigate trap formations is through a high-quality epitaxial growth where the films grown are done layer by layer to hopefully prevent the formation of defects within the lattice. While this prevents a significant amount of defect formation, there are still ways that defects can be formed within the crystal lattice. One way these defects can be formed in the lattice is strain of the grown layers. This strain is caused by a difference in the lattice constant of the previous layer and the grown layer. For the superlattice in the photocathode, the goal of the superlattice is to compressively strain the GaAs at a very specific strain rate to generate polarized photoelectrons. This strain relates to a GaAsP composition of $\text{GaAs}_{0.65}\text{P}_{0.35}$. Wafers of the correct crystal orientation and lattice constant are not readily available commercially. This means that the first step in generating a spin polarized photocathode is to create a final relaxed layer of the relevant lattice constant. This is done by slowly varying the Phosphorous content until the final target composition is reached in a fully relaxed state. This growth is called a metamorphic grading or pseudomorphic growth.

Before beginning to grow the proposed device structure, developing this metamorphic grading is necessary. These initial growths can be subdivided into two sections: preliminary composition calibrations and metamorphic grading optimization. Since the incorporation of As and P in the grown layer is not a direct relation to the vapor precursor phase, initial single composition layers were grown at the same temperature and 3 target compositions. These initial growths are key to initial calibrations for both growth rate and composition for the metamorphic grading.

Using this initial information, metamorphic buffers were grown. These metamorphic buffers must satisfy two criteria: the final layer composition (lattice constant) must be the same as the GaAsP composition within the superlattice and the final layer must be strain-free. To reach this goal, multiple variables were modified including wafer offcut, growth rate, grade rate, and growth temperature. Many of these parameters will change the incorporation rate of As and P so, while the initial single composition layers provide a sufficient starting point, metamorphic grading optimization is an iterative process to reach the final target composition with minimal strain.

3.2. Composition calibrations for $\text{GaAs}_x\text{P}_{1-x}$

Because of the nature of group V-based alloys, the stoichiometry of the gas phase vs the solid phase is nonlinear. Before developing metamorphic grading structures, doing single composition GaAsP alloys, and characterizing these alloys, allows to build a strong initial framework. For these purposes, three 200 nm $\text{GaAs}_x\text{P}_{1-x}$ layers were grown of 3 different phosphorous compositions. The three target compositions were $\text{GaAs}_{0.95}\text{P}_{0.05}$, $\text{GaAs}_{0.80}\text{P}_{0.20}$, and $\text{GaAs}_{0.65}\text{P}_{0.35}$. These layers were analyzed via Nomarski microscopy, coupled HRXRD, and spectroscopic ellipsometry.



Figure 3.1 Images from Nomarski microscopy of the 3 different $\text{GaAs}_x\text{P}_{1-x}$ composition films (phosphorous content increasing from 0.05, to 0.20 to 0.35 from left to right).

As the Nomarski images shows (Figure 3.1), as the phosphorus composition increases, the surface becomes more non-uniform. This is because, as the phosphorus content increases, the difference between lattice constant of the grown film and the substrate increases, thus defects are more likely to form. The point at which defects will begin to form in a film is known as the

critical thickness. Once the film thickness surpasses the critical thickness, relaxation will begin to occur along with various crystallographic relaxation.

Along with initial Nomarski measurements, coupled X-Ray diffraction scans were performed (Figure 3.2). Using these, preliminary thickness and compositional measurements can be obtained.

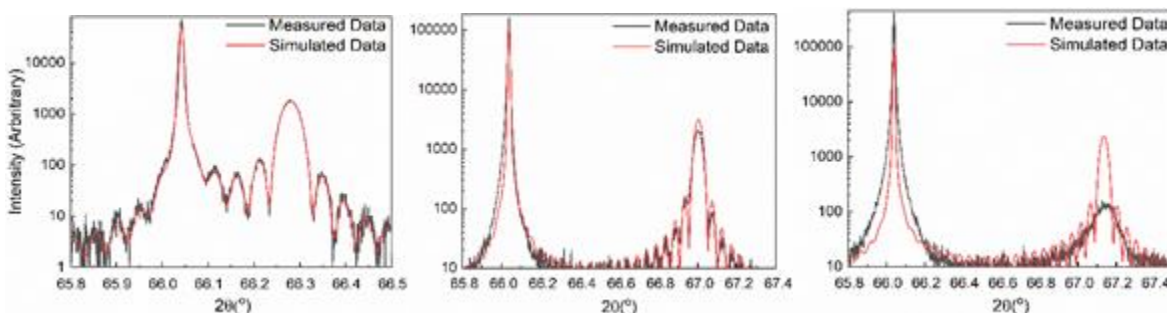


Figure 3.2 Coupled X-ray diffraction measurements on three $\text{GaAs}_x\text{P}_{1-x}$ films (phosphorous content increasing from 0.05, to 0.20 to 0.35 from left to right).

Two key peaks can be examined in the coupled x-ray measurements (Figure 3.2). First, the leftmost peak, is the peak of the GaAs substrate, and the secondary, lower peak is the peak related to the grown film. As the phosphorous composition increases, the quality of the second peak lowers and the interference fringes begin to disappear. These interference fringes are indicative of a high-quality epitaxy film. Their absence implies that there is a drop in film quality due to relaxation with the critical thickness. One of the key challenges of the decrease in the interference fringes observed in the high phosphorous ratio was a low parameter uniqueness of the fit. To verify its composition and other properties, other measurements were necessary.

Because the fit of the $\text{GaAs}_{0.65}\text{P}_{0.35}$ was poor via XRD, the thicknesses and composition of all three grown layers were also verified using spectroscopic ellipsometry. Using spectroscopic ellipsometry, it is possible to measure the thickness of the absorbing portion of the film, extract, optical properties, and approximate compositions using reference data (Figure 3.3).

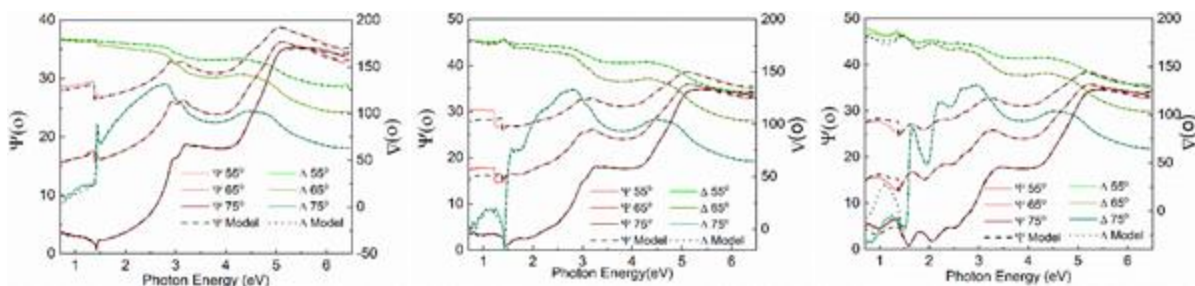


Figure 3.3 Ellipsometry data of the three different grown $GaAs_xP_{1-x}$ samples.

Figure 3.3 illustrates the psi and delta measurements for the three films obtained by spectroscopic ellipsometry. The dotted and dash lines show the fitted data from the ellipsometry models. Except for where GaAs is transparent, the model is in excellent agreement with the measured data. While there is slight disagreement with the XRD data, the thicknesses measured in these data are self-consistent and are summarized in Table 3.1.

Table 1 Results of Single Layer GaAsP Growths

Target Phosphorous Composition (%)	Calculated Phosphorous Composition (%)	Thickness from XRD (nm)	Thickness form Ellipsometry (nm)
5	4.7	224	218
20	19.9	218	221
35	33.9	220	216

As Table 1 shows, there is some slight variance between the XRD-derived and ellipsometry-derived fits, probably due to the drop of uniqueness the XRD measurements fit.

Using the Ellipsometry analysis, it is also possible to extract the real and complex dielectrics of the deposited layers. The shape of the complex dielectric functions agrees well with all of them shifting towards higher energy with higher phosphorous content. When compared to the literature values, the key optical transitions are trending towards GaP. One potential concern observed in the $GaAs_{0.65}P_{0.35}$ film is the weakening of the E_0 transition. When typically related to band gap, the strain and relaxation in the higher strained film provide a potential cause for this.

While initially done to corroborate thickness and composition measurements, additional information can be extracted from the ellipsometry simulations. Since a general oscillator

methodology was used, information regarding the optical constant of GaAsP was extracted. Even more than that, information about specific optical transitions was also obtained.

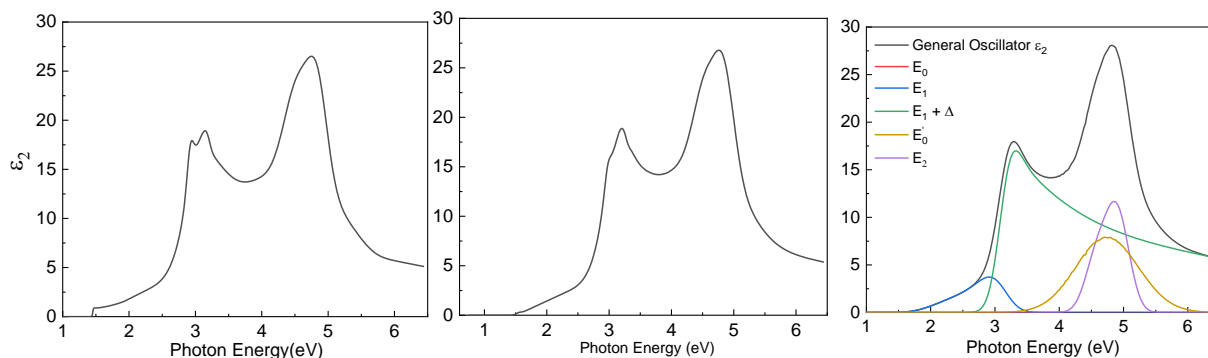


Figure 3.4 Complex dielectric constant for GaAs_xP_{1-x} film, with phosphorous composition ranging from 0.05 to 0.35. The 0.35 Sample shows the full deconvolution of the oscillators

Figure 3.4 shows the dielectric constants of all 3 as-deposited films as well as the deconvoluted oscillations for their respective optical transitions. For all 3 films the band gap transition E_0 is relatively weak, but is then followed by a stronger E_1 transition.

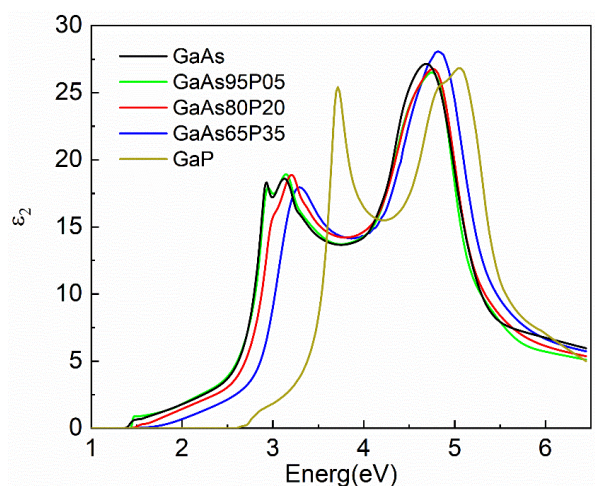


Figure 3.5 Complex dielectric constant of the three model films with reference measurements for GaAs and GaP.

Figure 3.5 shows the extracted dielectric constant along a b-spline fit of a GaAs wafer and a reference GaP wafer. All the key optical transitions within the deposited films are correctly transitioning towards that of GaP.

3.3. Metamorphic layer calibration

Using the initial composition calibrations, metamorphic buffer layers were grown on GaAs wafers. Nomarski microscopy and reciprocal space mapping were performed to determine both the strain and composition. To achieve these key design goals, multiple metamorphic gradings were grown to fully optimize both parameters.

Table 2: Summary of Metamorphic Grades Grown During Calibration with targeted properties

Run	Growth Temp (°C)	Wafer(s)	MMG Delta [%P]	Layer Thickness [nm]	MMG Steps	PH ₃ /AsH ₃ of final layer	Growth Rate [μm/hr]	Zn/GIII of MMG	Targeted OSL [%P]
21R100	650	UID (100) 2° <111>A (-3) UID (100) on-axis (-4)	5	1000	9	3.360	9.8	0.127	43
21R140	650	UID (100) 2° <111>A (-2) UID (100) on-axis (-4)	5	1000	9	3.360	9.8	0.127	40
21R200	650	UID (100) 2° <110> (-1)	5	1000	9	1.286	9.8	0.127	40
21R201	730	UID (100) 2° <110> (-1)	5	1000	9	1.286	9.8	0.127	40
21R269	650	p (100) 2° <110> (-1) UID (100) 2° <110>	5	1000	9	7.143	9.8	1.27E-02	40
21R270	730	p (100) 2° <110> (-1)	5	1000	9	2.000	9.80	0.192	40
21R277	730	p (100) 2° <110> (-1)	5	1000	9	2.000	3.06	0.578	40
21R327	730	UID (100) 2° <111>A (-3) UID (100) 2° <110> (-4)	2.5	500	15	2.083	9.800	0.192	40
21R333	730	p (100) 2° <111>A (-1)	2.5	500	15	2.083	9.800	0.192	40
22R064	730		2.5	500	15				40
22R065	730		2.5	500	15				40

Table 2 shows a summary of the calibration runs for the metamorphic gradings. Runs highlighted in yellow are metamorphic calibration runs discussed in detail, and ones in green are completed, measured devices (discussed in chapter 4). One of the challenges of initial growth campaigns is that, while runs are highly reproducible with the same run conditions, there is variance between

specific MOCVD reactor systems. Initial parameters for a metamorphic grading were utilized from other MOCVD systems and, using initial calibration runs, the first metamorphic gradings were grown [21].

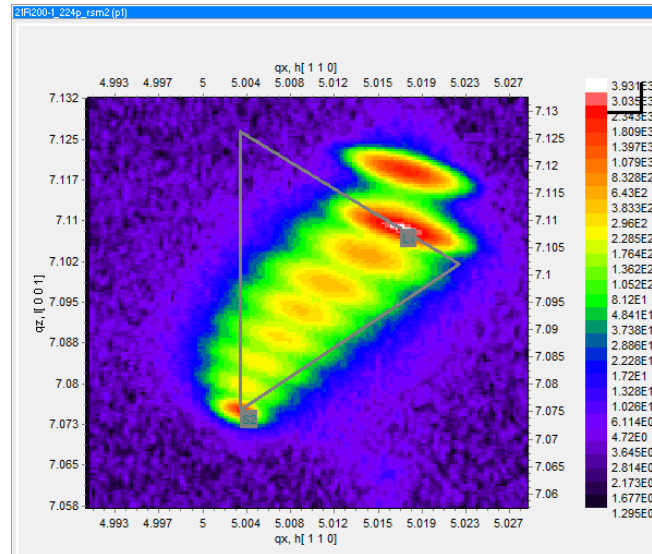


Figure 3.6 Reciprocal space mapping for the initial metamorphic layer calibration (21R100)

The reciprocal space map for the first attempted metamorphic grading (21R100) is shown Figure 3.6. The resulting growth had a lower phosphorous grading than expected. Instead of having the intended grade rate of 5%, the grade rate was only 2.4%. This means the final surface concentration was 17.5%, half of the targeted composition. This lower step size is due in large part to the significant amount of Zinc precursor needed to reach the target doping concentration. Effectively, in the previous calibration runs, the GaAsP films were grown undoped. For the actual device structure, a high p-type doping is necessary to facilitate sufficient band bending to allow for negative electron affinity to occur. While the metamorphic grading is far from the surface, having a highly-doped p-type metamorphic grading will prevent diffusion of the p-type dopant out of the superlattice.

The high concentration of zinc precursor during growth results in two specific challenges. First, the Zinc changes how substituent elements incorporate into the final grown film. Since arsine

already preferentially incorporates better than phosphine, the high levels of diethyl zinc can exacerbate this [34]. Many studies have shown the impact of zinc precursor concentration and variation in film properties for III-V materials. At lower temperatures, Diethyl zinc can be beneficial to growth rate but, at higher temperatures, it is detrimental [35]. These two challenges taken together resulted in a lower-than expected phosphorous composition in the metamorphic grade. The most simple process to increase the phosphorous composition in the grown film is to increase the growth temperature. This is because, while zinc has an impact on the incorporation of phosphorous in the final film, the main physics that govern the incorporation of these two species are reaction kinetic based. In the gas phase, PH_3 is a more stable molecule. This means that it will pyrolyze (thermally decompose) at a higher temperature than AsH_3 . The growth surface temperature was increased from 650°C to 730°C to increase the amount of Phosphorous in the final film [36].

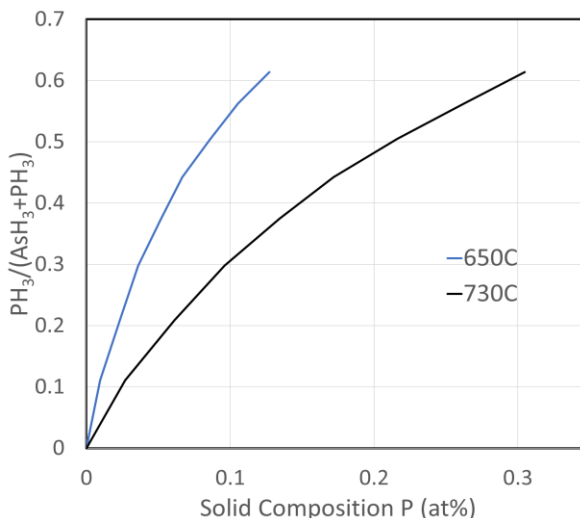


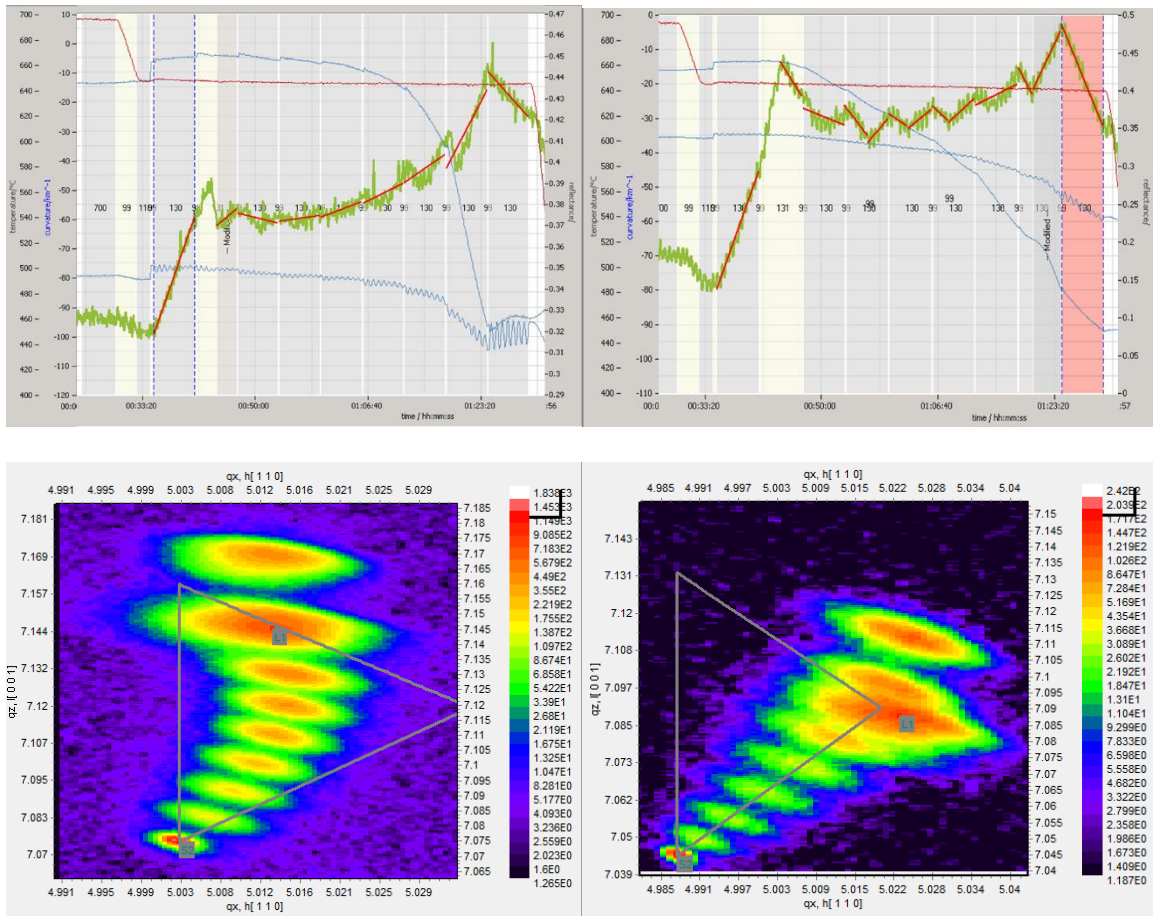
Figure 3.7 Gas ratio as a function of Phosphorous composition in the solid for various substrates temperature as extracted from two different metamorphic grading runs (21R200 and 21R201).

Figure 3.7 shows the incorporation of phosphorous in the final grown layer compared to the gas phase ratio. At the growth temperature of the initial metamorphic grade (650°C), even at significantly higher gas phase compositions, the final phosphorous composition in the film is

significantly lower than the targeted. With the increase in temperature to 730°C, phosphorous incorporation is sufficient to reach the final target composition.

3.4. Metamorphic layer optimization

For the metamorphic layer optimization growths, temperature, growth rate, and grade rate were varied in an attempt to get a fully relaxed final layer with the intended final composition. Because temperature was consistently varied to improve relaxation, calibrations of Phosphorous incorporations were done simultaneously with relaxation engineering. Multiple wafer offcuts were also used to further facilitate relaxation (see Table 3.2).



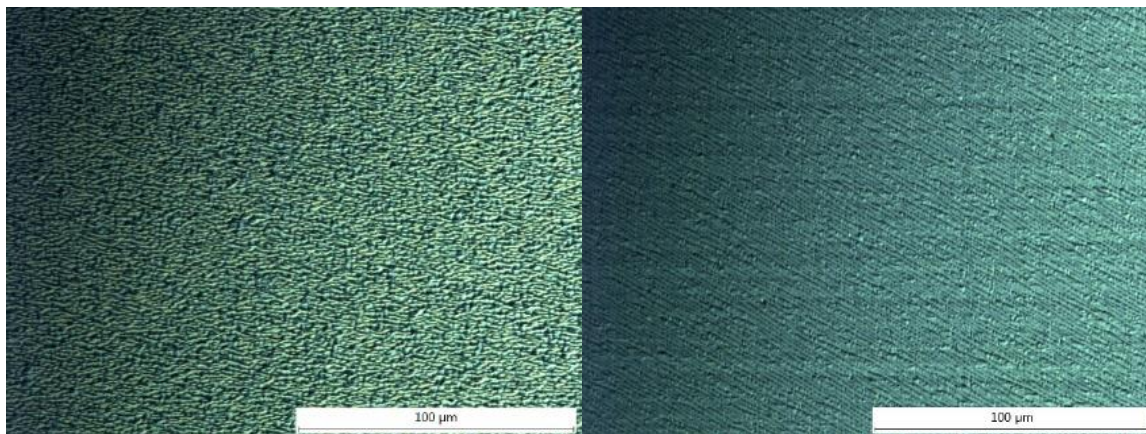


Figure 3.8 Telemetry, HRXRD and Nomarski results for a wafer (left) with 1° offcut in the (110) direction and (right) on axis (21R100)

The telemetry, reciprocal space mapping and Nomarski images for the first metamorphic grade are shown Figure 3.8. The left column is for a (100) GaAs wafer with a 1° offcut in the (110) direction and the one on the right is on-axis (run# 21R100). Looking at the telemetry, the curvature in the offcut sample increases significantly, which implies an increase in strain. When examining the RSM of the sample, as subsequent layers are grown an increase in strain can be observed. The impact of the strain in the offcut wafer can be seen in the poorer quality of the Nomarski image. Compared to the relaxed on-axis wafer, the surface is much rougher and course. While the on-axis wafer is overrelaxed, this is due, in large part to the low phosphorous composition in the film. While the target final composition had a P/V ratio of 0.35, the final ratio here was only 0.18. Even though the film was fully relaxed, there was significantly less strain that needed to undergo final relaxation compared to target compositions.

The next growths were done to refine the As to P ratios in the grown films (compared to the 0.18 obtained in the previous run). This was done by increasing growth temperature to 730°C (Figure 3.9). Higher temperatures increase overall phosphorous compositions and the higher kinetic energy within the film should facilitate relaxation (run # 21R201).

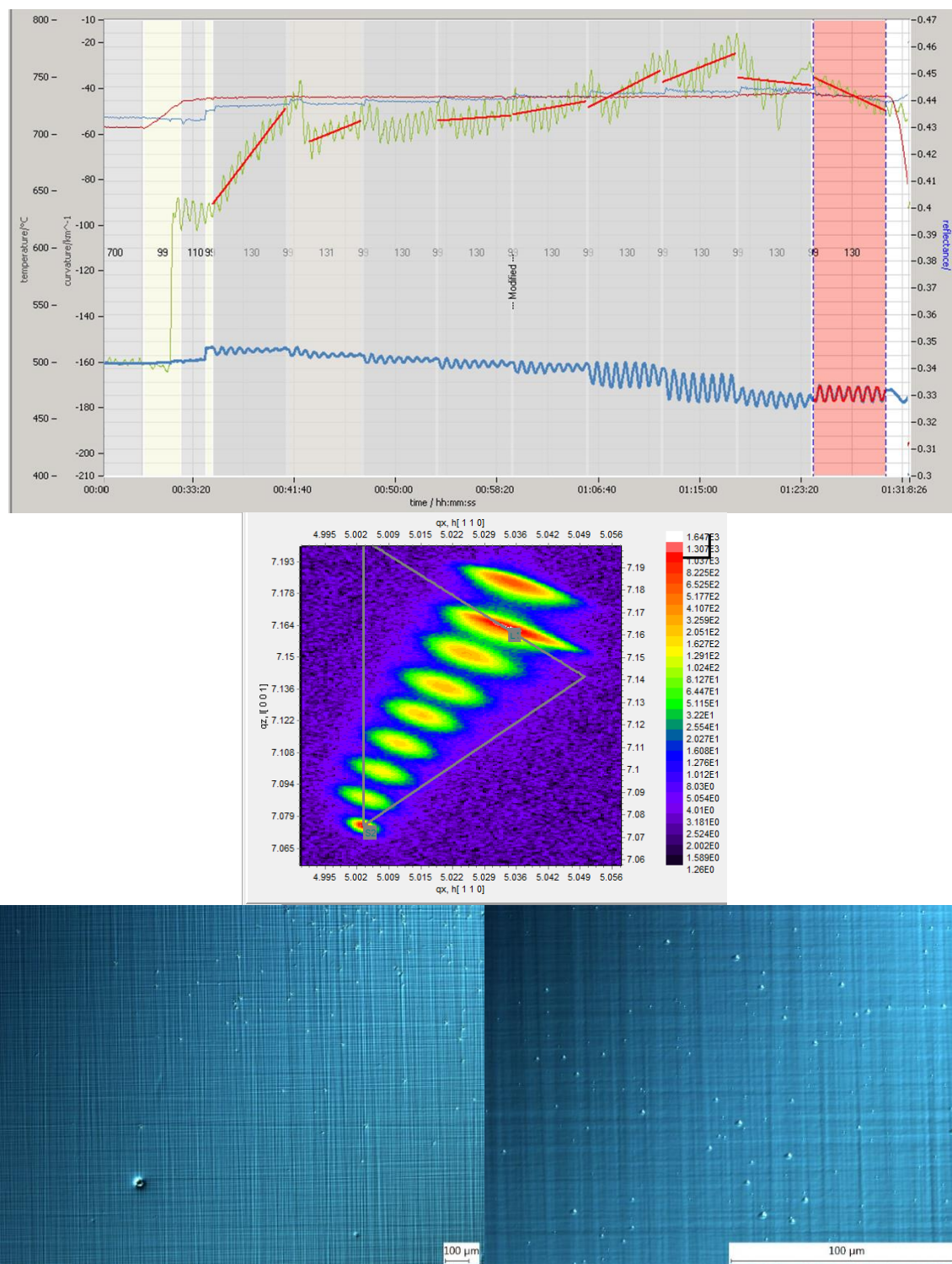
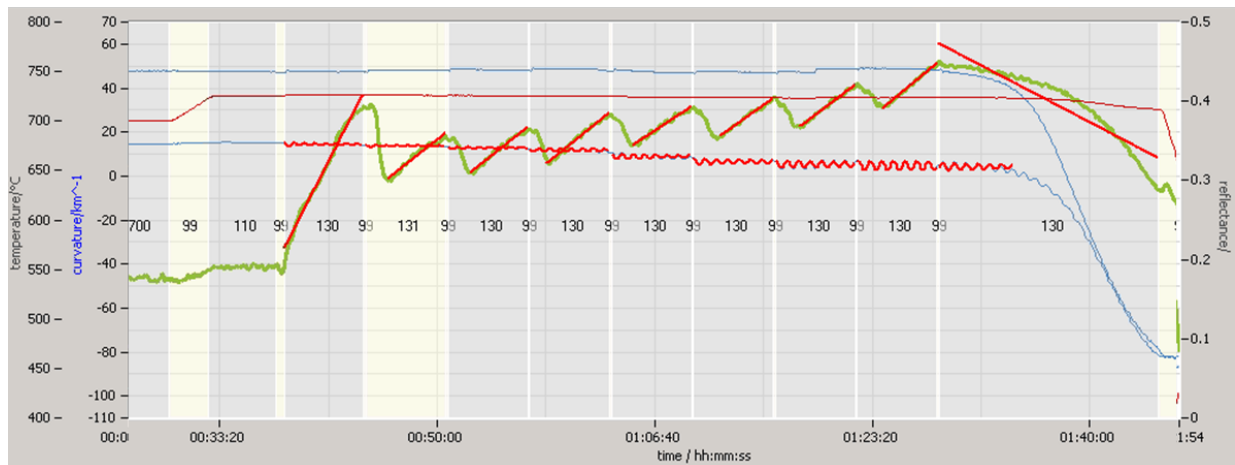


Figure 3.9 Telemetry, HRXRD and Nomarski results for growth offcut wafer in 21R201

Compared to the previous calibration runs, the RSM shows a more strained final layer. This increase in strain is due to the higher temperature increasing the phosphorous composition. The increase in phosphorous composition in the film results in a larger lattice mismatch thus more strain that needs to be relaxed. Using the data from these and previous runs, the final Phosphine and Arsine ratios were calculated to reach the final composition for the strained GaAs photocathode.

Now that the final composition was reachable, the next goal was to grow a device that was both relaxed and specular. If the wafer is not highly reflective, the incident light energy will scatter or not properly propagate into the photocathode. If the light does not propagate completely normal to the surface, any noncircular polarized light will excite nonpolarized light which will cause a decrease in polarization. Because target compositions were successfully obtained, all subsequent metamorphic grading tests contained a complete device architecture. This was done because, if target properties were obtained in the metamorphic grading, it could be tested immediately.



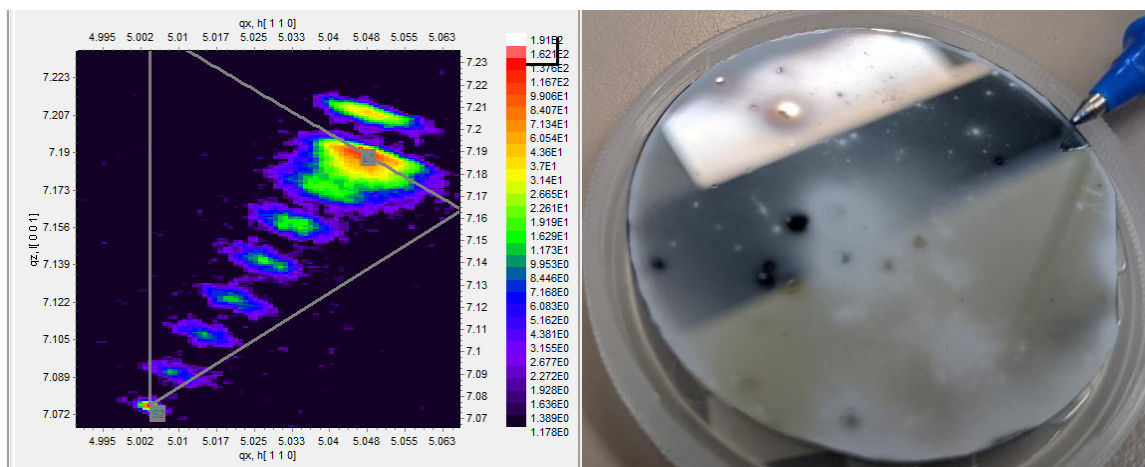


Figure 3.10 Telemetry, HRXRD and image results for offcut wafer in 21R270

21R270 is a continuation of 21R201 with the key differences being an increase Zn flow rate and a varied AsH_3/PH_3 gas ratio to compensate for the increase in Zn precursor (Figure 3.10 and Table 3.2). While the film is still not fully relaxed, the final film surface is starting to show regions of high specularity. Unique to this run, there is still a decent amount of strain. Instead of this strain resulting in a periodic structure that could be observed through Nomarski, much of the non-uniformity is macroscopic and can be seen directly through visual inspection (Figure 3.10). Because the surface of the wafer is so inhomogeneous, photoluminescence (PL) mapping was done instead to examine compositional irregularities in the grown layers (Figure 3.11). This works by examining the difference in absorption and luminescence of various wavelengths of light in specific localized portions of the wafer. Using photoluminescence, it is possible to examine where the non-uniformities chemically are in the wafer and the approximate composition of the near surface region.

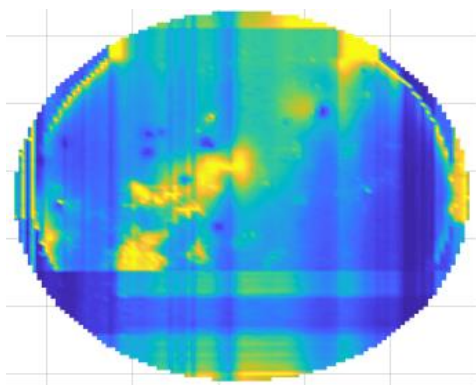


Figure 3.11 Photoluminescence mapping for the sample shown in figure 3.10 The heat map shows the average PL intensity

As the PL mapping shows, the localized non-uniformities within the wafer have a significant impact on the PL response. This is for two distinct reasons. In regions of high reflectivity, not as much light will be absorbed into the wafer compared to the rough regions. These regions of higher roughness will scatter more light into the sample thus have a higher PL response. Second, is composition variation. Regions with a higher phosphorous composition (higher bandgap) will have a lower intensity than areas with a lower phosphorous ratio (see figure 3.5).

At this point, final target compositions had been reached, but full relaxation had not been reached. To reach final relaxation, three key parameters were changed: growth rate, wafer offset, and grade rate.

By changing the growth rate, the goal was to give the film time to resolve strain and relax. To test the impact of growth rate on relaxation, the growth rate was decreased from 9.8 $\mu\text{m/hr}$ down to 3 $\mu\text{m/hr}$ (run #21R277, Table 3.2). As Figure 3.12 shows, the decrease in growth rate had a significant, adverse effect. As the RSM shows, lowering the growth rate results in a significantly higher strained. The final surface is also extremely rough and non-uniform. Under SEM, the random surface observed in Nomarski can be seen clearly as crystallographic facets that manifest on the surface due to the high degree of strain.

each step will be lessened. To improve relaxation potentially further, the offcut of the wafer was changed from the (110) direction to the (111) direction. This was done because the (111) step align better with the glide angle of defects within GaAs [37]. To test the impact of the metamorphic grade rate, the difference between composition steps was cut in half to 2.5%. To maintain a similar metamorphic grade thickness, the layers within the metamorphic grade were also cut in half to 500 nm (Run #21R327, Table 3.2).

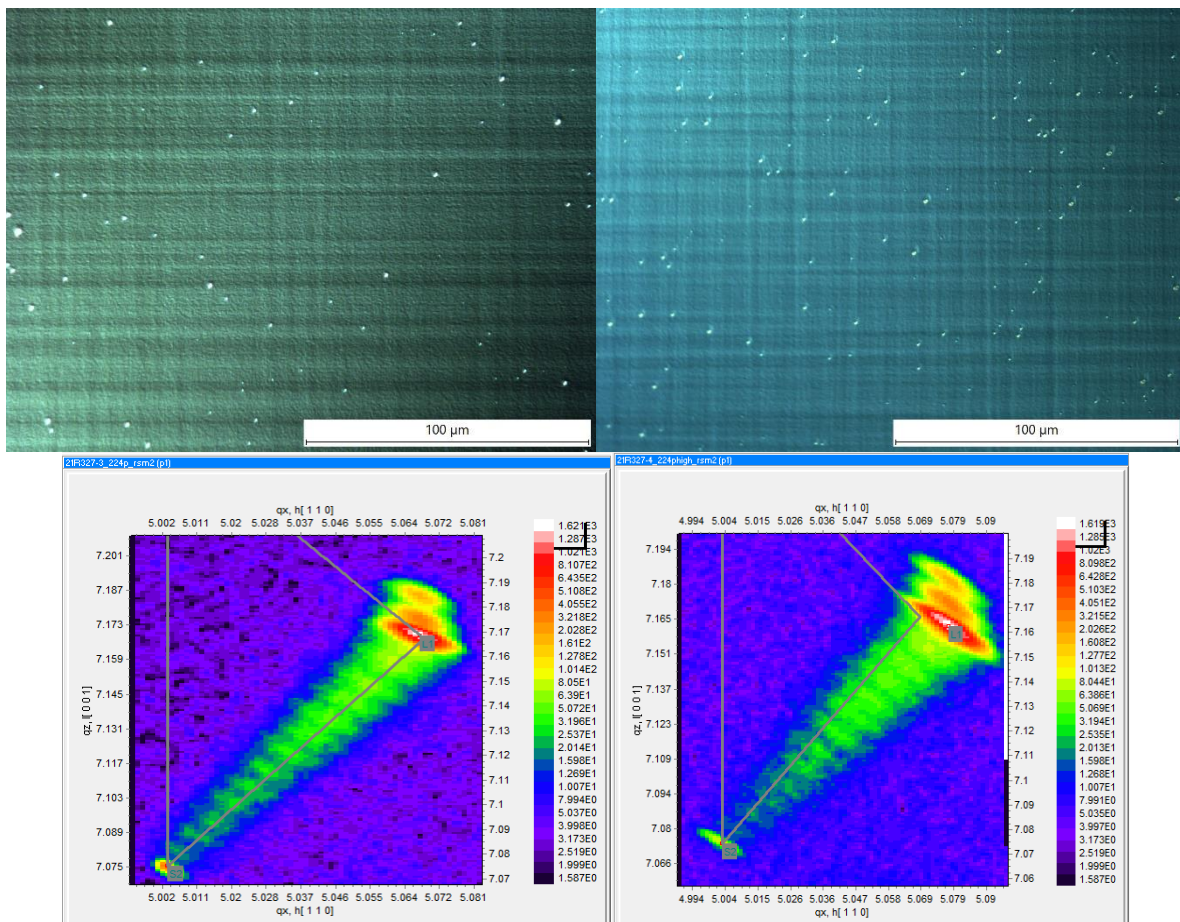


Figure 3.13 Nomarski and RSM of Run 21R327 metamorphic gradings with (111) offcut (left) and on-axis (right)

As Figure 3.13 shows, the metamorphic grading is fully in line with the relaxation line in the reciprocal space map. The final buffer relaxation in the (111) offcut wafer is 98.8% and the resulting buffer should provide an ideal candidate for a full device. This same metamorphic

grading was used to create a full device in 21R333; that run will be discussed in detail in the subsequent chapter.

Chapter 4: Superlattice Growth and Device Characterization

4.1. Introduction

As Chapters 2 and 3 have demonstrated, after initial compositions were calibrated, fully relaxed tensile metamorphic layers were grown. To complete a photocathode, an additional 2 μm of $\text{GaAs}_{0.65}\text{P}_{0.35}$ was grown. This was done to resolve any remaining defects and improve final surface quality. After that final buffer layer growth, a $\text{GaAs}/\text{GaAs}_{0.65}\text{P}_{0.35}$ superlattice was grown. This superlattice was first fabricated and analyzed on GaAs substrates via XRD. XRD will confirm that the superlattice has the correct periodicity (layer thickness). After the fidelity and the doping of the superlattice is verified, photocathodes will be completed and tested.

4.2. $\text{GaAs}/\text{GaAs}_{0.65}\text{P}_{0.35}$ superlattice growth

The general growth pattern for a superlattice is as follows: first the Trimethyl Gallium and hydride are introduced. Then, the precursor gases are purged with hydrogen. This is done to ensure a high-quality interface between the two different layers. If the growth was more continuous, the superlattice interfaces would lose fidelity. After the hydrogen gas purges out the remaining precursors, the precursors for the next growth phase are introduced. This gas pulsing is performed until the targeted number of layers is deposited.

Initial superlattices were grown directly on two different GaAs wafers (on-axis and (110) offcut). This was done to ensure both proper doping calibrations and layer fidelity. Two different wafer offcuts were used to examine the potential impact of the offcut on superlattice quality. While offcuts may be detrimental to the quality of the superlattice, they can help significantly with metamorphic grade relaxation. Since initial devices were grown on a (110) offcut substrate,

understanding how the offcut could affect superlattice quality was key for substrate selection in the future.

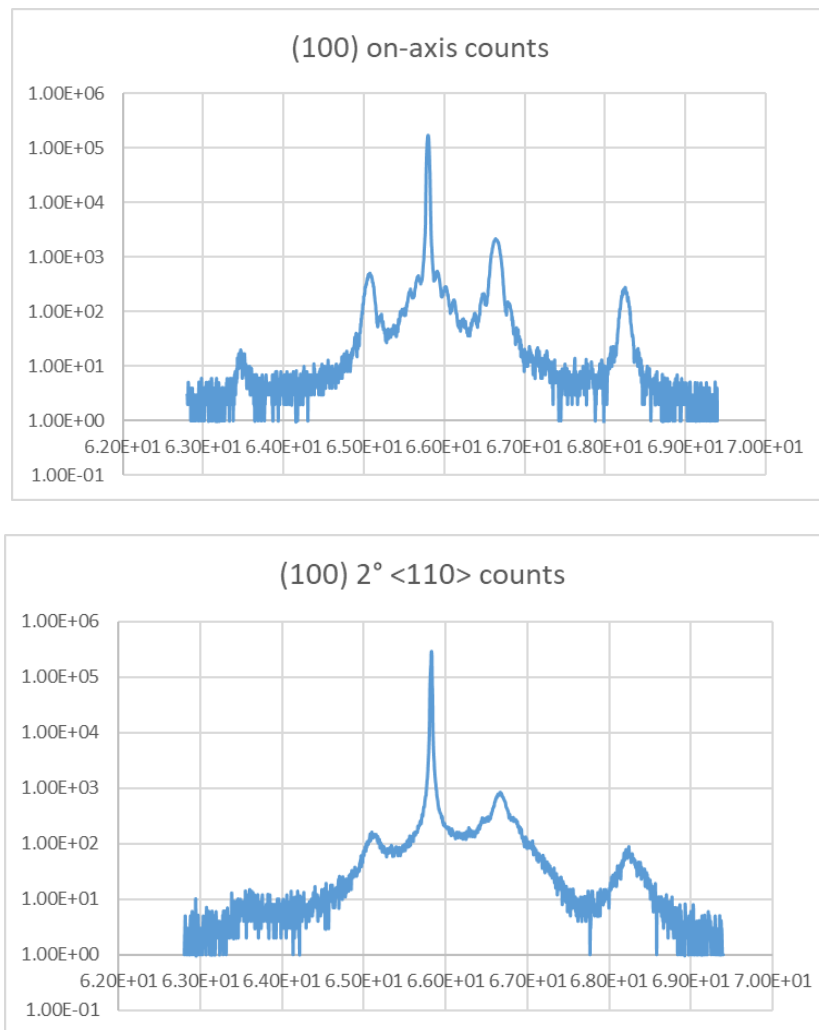


Figure 4.1 XRD of two GaAs/GaAs_{0.65}P_{0.35} superlattices grown on (100) GaAs on-axis (top) and on-axis with 2 degree offcut in the (110) direction (bottom)

The XRD patterns in Figure 4.1 show the superlattices grown on on-axis and offcut wafers. The on-axis wafer has significantly more interference fringes than the offcut growth (as seen near the peak at 66 degree). This implies that the superlattice in the on-axis growth is of a higher quality. While the on-axis superlattice is better, the offcut superlattice was still of reasonable quality and

should be a better candidate for metamorphic grading relaxation. For that reason, initial devices were grown on offcut wafers.

4.3. Initial device characterization

After the optimization of the metamorphic grade, device characterization was performed. Before testing a superlattice cathode, a bulk GaAs cathode was characterized. The procedure for characterization is outlined in Section 2.5.7. After verifying the Mott polarimeter was functioning properly, a superlattice photocathode was introduced. For activation, the photocathode was annealed at 560°C. This was done to prevent interdiffusion within the superlattice and As dissociation from the surface [38]. To ensure verification of spin polarization within the grown devices, measurements were done both at Brookhaven National laboratory and JLab.

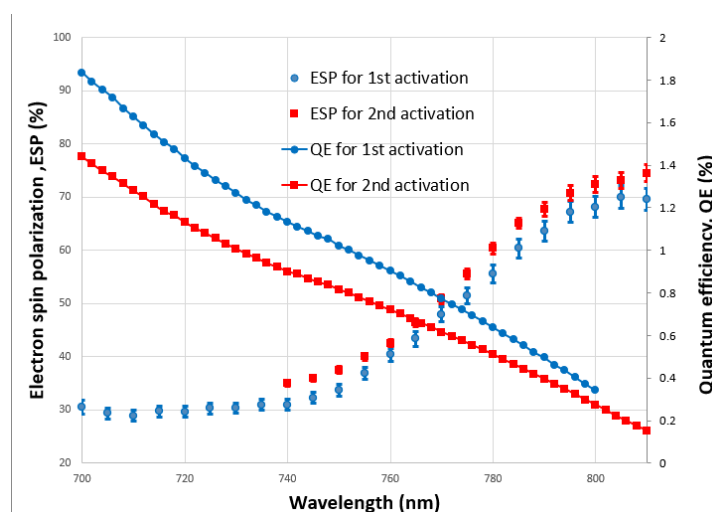


Figure 4.2 Electron spin polarization and quantum efficiency as a function of wavelength for our initial device (run# 21R333)

Figure 4.2 shows the first successfully completed and measured device (run # 21R333). The devices have the low characteristic quantum efficiency of strained superlattice photocathodes with a polarization greater than 70%. While this first result is promising there are deficiencies with this device. Compared to other strained superlattice devices, the wavelength of peak polarization is red-shifted and broad [4]. This implies issues with either the superlattice, surface or both. Examining Figure 4.3, there is a significant amount of surface dimpling. This dimpling could be

potential signs of depolarization for the electrons or scattering of the laser. The red shift of the peak polarization also implies that the strain within the structure is lower than expected. This can be inferred because with less strain the heavy hole light hole splitting energy will be smaller and closer to the band gap of GaAs.

4.4. Device Refinement

While a strained superlattice photocathode was successfully developed, improvements and device refinement are necessary. While the final goal is to implement a distributed Bragg reflector (DBR), additional work should be done first to improve general device performance. To examine potential deficiencies with the superlattice periodicity, TEM was performed. With TEM inhomogeneities within the superlattice both due to surface nonuniformities and irregular layer thicknesses can be examined.

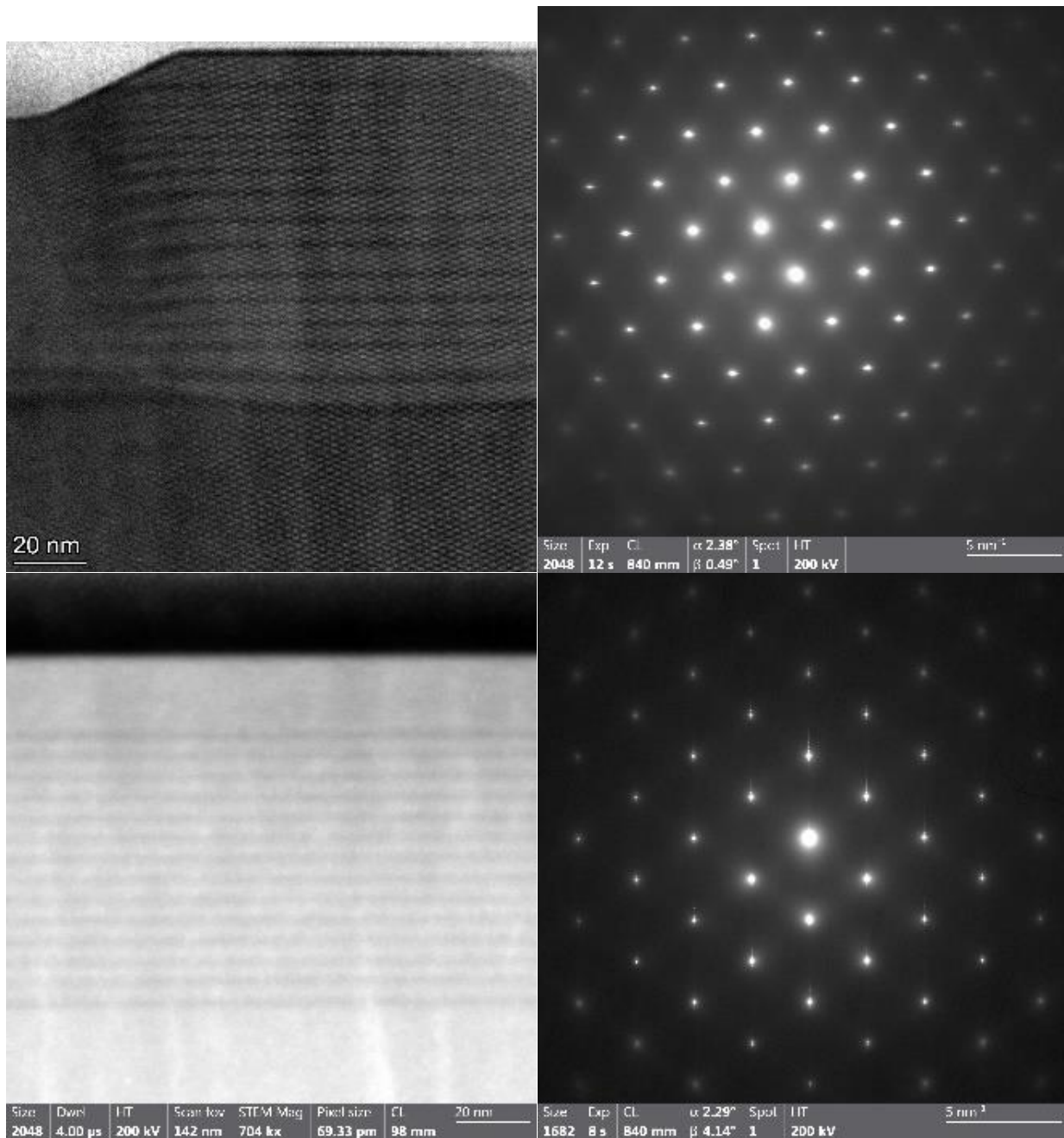


Figure 4.3 Transmission electron microscopy of the superlattice on the first fully completed device (top) compared to a sample superlattice grown on on-axis GaAs (bottom)

Figure 4.3 Shows the superlattice of run# 21R333 compared to a standard GaAs/GaAsP superalltie grown on on-axis GaAsP. As the TEM shows, the layers within the superlattice are fairly nonuniform (the dark regions are GaAs and the light regions are GaAsP). When approaching one of the dimpled regions, the layer fidelity appears to disappear completely. This will cause a net drop in polarization because the radius of the laser is large relative to the size of the dimpling.

The laser size will result in averaging the polarization of these regions with no superlattice and the irregular superlattice. This will cause a net loss in the spin polarization in the cathode.

To determine if these irregularities/dimpling are due to the metamorphic grading and offcut or the superlattice recipe itself, a TEM of the same superlattice was performed on the same superlattice grown on on-axis GaAs. In this growth, the layers were highly periodic with excellent fidelity. This implies that the offcut was having a greater impediment on superlattice fidelity than initially expected.

To better understand the quality of the device surface, AFM was performed. By using AFM, information about the growth can be ascertained by looking at if the grown film has a strongly imposed direction. AFM will also provide additional insight into surface dimpling if any are present.

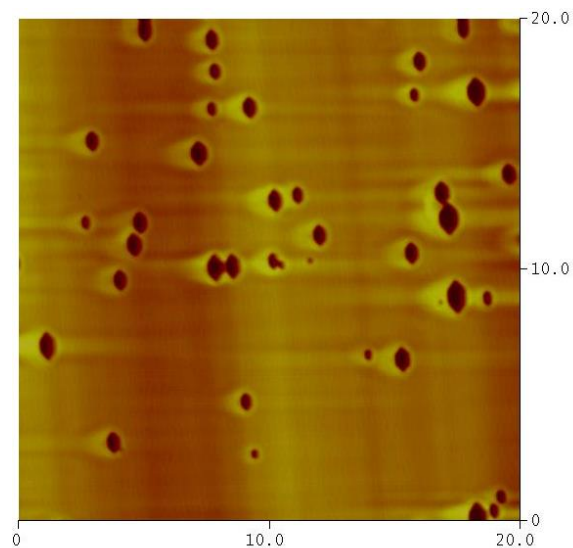


Figure 4.4 Atomic Force Microscopy image of the superlattice on top of a full device with offcut wafer (copy of recipe from run #21R333)

AFM measurements (Figure 4.4) done on top of a full device show two distinct characteristics. First, there is an imposed orientation in the growth. This is due to the initial offcut in the wafer. Second, there is a significant amount of surface dimpling. These dimples are deep and is one of the key contributing factors of the non-uniformity in the final device properties.

To improve the device quality both the superlattice and surface quality need to be addressed. As the initial XRD of superlattice showed, the superlattice on an on-axis GaAs substrate was a much higher quality one. The first step is to transition from a wafer with an offcut to an on-axis one. With minor modifications to the metamorphic grading developed in 21R327 a fully-relaxed high quality metamorphic grade was developed, .

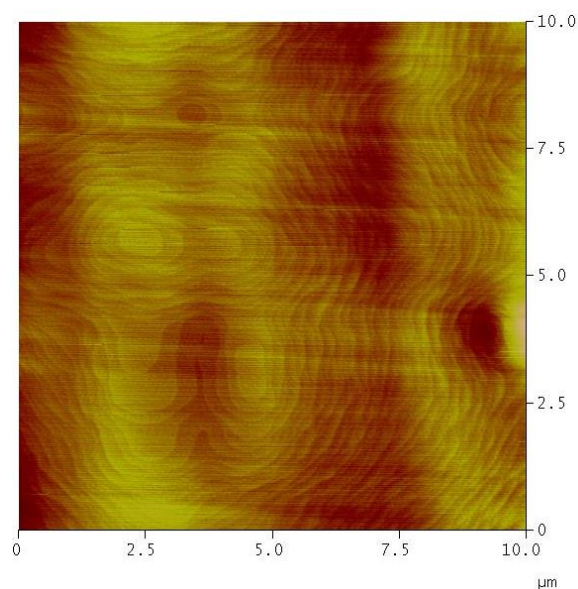


Figure 4.5 Atomic Force Microscopy image of the superlattice on top of a full device with on-axis wafer (run22R064)

Figure 4.5 shows the AFM image of a superlattice grown on top of full device with an on-axis (100) GaAs wafer (run 22R064). Unlike the (111) offcut growth, there is no imposed growth direction. This results in a “layer cake” morphology since initial layer nucleation occurs at steps that are randomly distributed throughout the wafer. While the surface looks much more non-uniform, it is much smoother, and, unlike the offcut wafer, the surface dimpling is not as significant. The other growth modification done to potentially improve surface quality is varying the V/III gas ratios. This was done to ensure an even greater excess of the hydride component was present during the reaction. Because the pyrolysis and reaction of AsH_3 and PH_3 is one of the more kinetically challenging processes during growth, by increasing their relative composition, the

reaction with the absorbed metallic precursor should result in a faster reaction thus a more smooth surface.

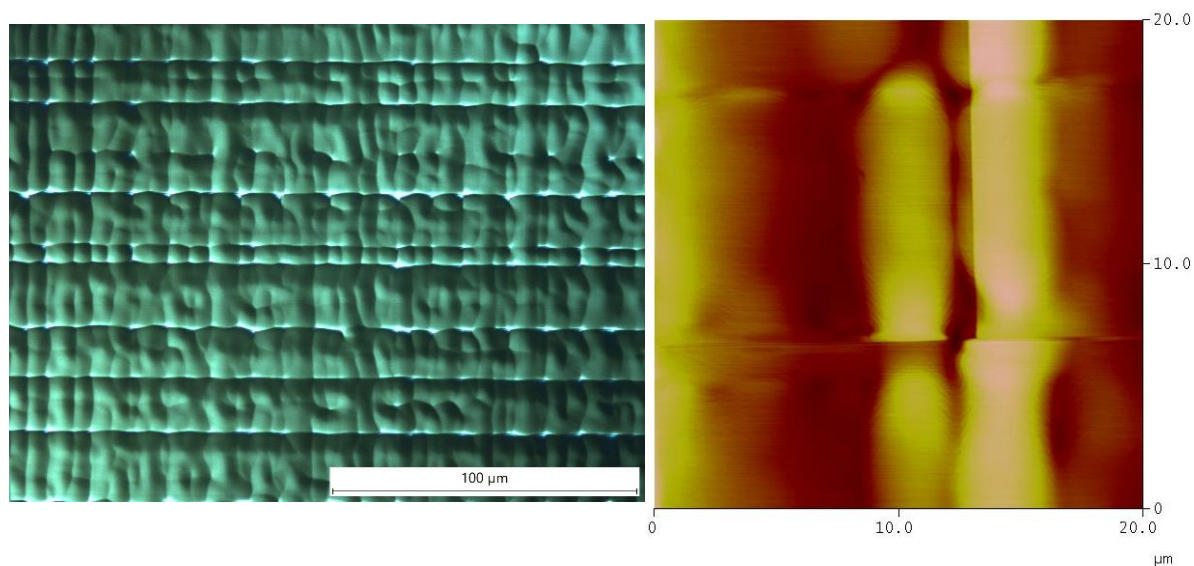


Figure 4.6 Nomarski image and Atomic Force Microscopy image of improved superlattice photocathode (run 22R064)

As the Nomarski image for run 22R064 shows (Figure 4.6), there is a textured but uniform structure. When examining these areas of texture under AFM, the facets are around 25 nm deep, but compared to the dimpling observed in the offcut wafers, these facets are much more continuous. Under standard visual inspection, the photocathodes appear to have a highly-specular, but slightly textured, appearance. Unlike the offcut wafers, there was no region of fogginess on the surface of the photocathode. With the surface issues resolved, TEM/EDS was performed on finished photocathodes (Figure 4.7).

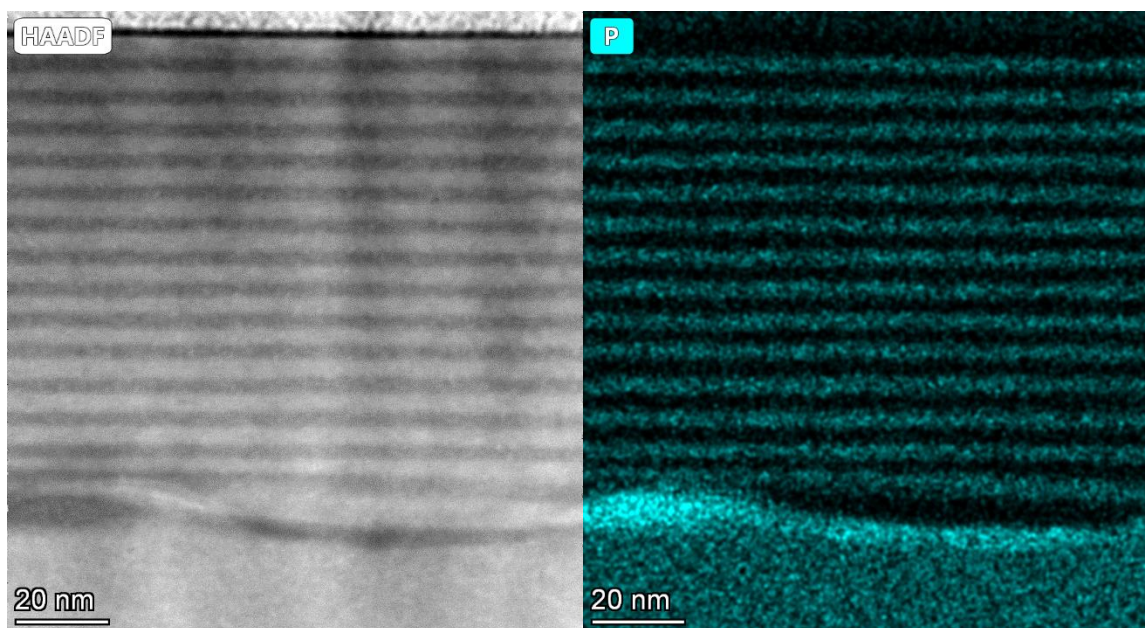


Figure 4.7 TEM imaging and EDS on photocathode with on-axis wafer (run 22R064)

Similar to the surface, the quality of the superlattice was also much improved. The superlattice has periodic behavior that is expected with the known superlattice recipe. Examining the EDS, outside of the initial buffer superlattice interface, there appears to be little interdiffusion of phosphorous into the superlattice layers.

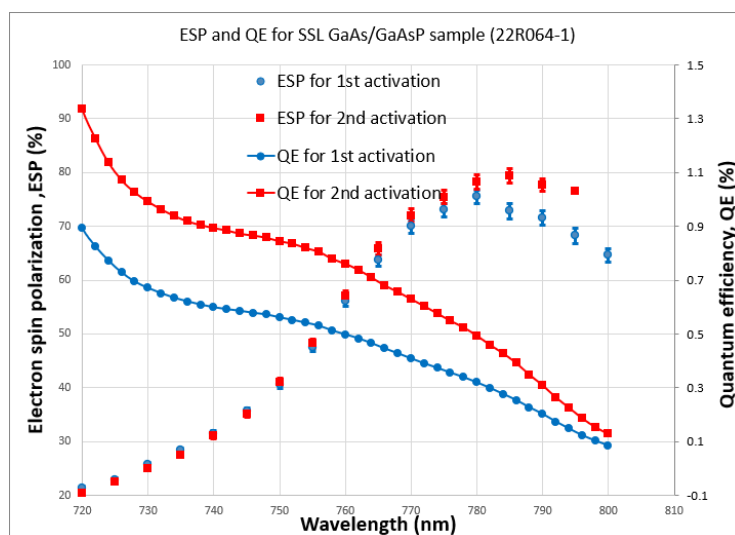


Figure 4.8 Electron spin polarization and quantum efficiency as a function of wavelength for improved superlattice photocathode (run 22R064)

Figure 4.8 shows the device characteristics for the new and improved photocathode (run 22R064). In this device, the spin polarization is increased by 10% and the quantum efficiency more than doubled at the point of peak polarization. While higher polarizations have been reported, this combined level of quantum efficiency and polarization is quite good, which is a promising first result for MOCVD-grown strained superlattice photocathodes. Because the superlattice layers are more uniform, the strain in the GaAs layers is more uniform. This more uniform strain in the GaAs has resulted in both a tightening of the polarization peak and a blue shift in the point of peak polarization.

4.5. Distributed Bragg Reflector

While refinement of the superlattice can facilitate increases in both polarization and quantum efficiency, the key challenge to the low quantum efficiency in this device architecture is the active area within the device. In a strained superlattice photocathode, only the GaAs layer photoemits. While the number of superlattice pairs can be increased, as electrons diffuse through the superlattice, depolarization occurs [39,40]. There is also a hard limit on the thickness of the device active region due to the thickness of the band bending region that causes negative electron affinity. Superlattice outside of that band bending region will not have negative electron affinity, thus photoemission either will not happen or be difficult.

There are several ways that quantum efficiency can be improved in optoelectronic devices, but many of these also pose unique problems. Two common ways to improve absorption is to improve external quantum efficiency via surface treatments. These come in two categories: surface texturing and antireflective coatings [41,42]. Unfortunately both of these are not feasible. Surface texturing will result in significantly lower polarizations because light not hitting normal to the surface will result in light propagating in the photocathode of a different polarization than the incident light. While antireflective coatings would result in more light entering the superlattice, the obligatory negative electron affinity surface requires very precise control of the surface chemistry.

These leaves us with one option: a distributed Bragg reflector (DBR) in the buffer layer. A distributed Bragg reflector is another type of superlattice structure, where materials of alternating refractive indices are deposited to create a highly reflective mirror [43]. The bandwidth location and width can be controlled through the thicknesses and number of periods. This DBR allows a second pass of incident light thus increasing quantum efficiency.

The first step of developing a DBR is material selection. Unlike in the photoemission region, lattice matched material is required. This limits us to two different compound semiconductors: AlAsP and InAlP. Because it has the greatest difference in refractive index relative to GaAsP, AlAsP is the ideal candidate material optically for the DBR [44].

Much like GaAsP, AlAsP has similar calibration challenges with PH_3 and AsH_3 . AlAsP has further complications due to its chemical stability. When AlAsP comes in contact with water vapor, it spontaneously and rapidly decomposes into Al_2O_3 and PH_3 [45]. This means that in order to do calibration runs, a sufficiently thick capping layer is necessary. The thickness of this capping layer can be complicated due to the properties of the AlAsP layer that is grown. To develop a high-quality calibration run, a metamorphic grading is grown. This is convenient because it includes multiple AlAsP layers with various AsH_3 and PH_3 gas ratios. In initial runs, the surfaces were highly irregular and the 100 nm GaAs capping layer was insufficient. This resulted in rapid oxidation of the film and the release of PH_3 gas within the glove box.

To create a more chemically stable DBR, InAlP was examined. While InAlP is not as good optically for a DBR, it provides several unique advantages over AlAsP. InAlP is much more chemically stable than AlAsP, because the addition of another group III constituent stabilizes the Al. The second key advantage is better group III precursor incorporation. The non-linearity of PH_3 and AsH_3 was a key challenge in developing the GaAsP buffer; if AlAsP was pursued similar challenges would be present. InAlP instead varies the group III composition, and group III precursors are more reactive, so they incorporate more closely to their gas phase. Since the Group III precursors are Trimethyl Indium and Trimethyl Aluminum, the difference in incorporation

between the two is not as severe. Any loss in optical performance seen by transitioning from AIAsP to InAIP can be mitigated by modifying the number of periods in the DBR or by varying DBR layer thicknesses (run # 22R065).

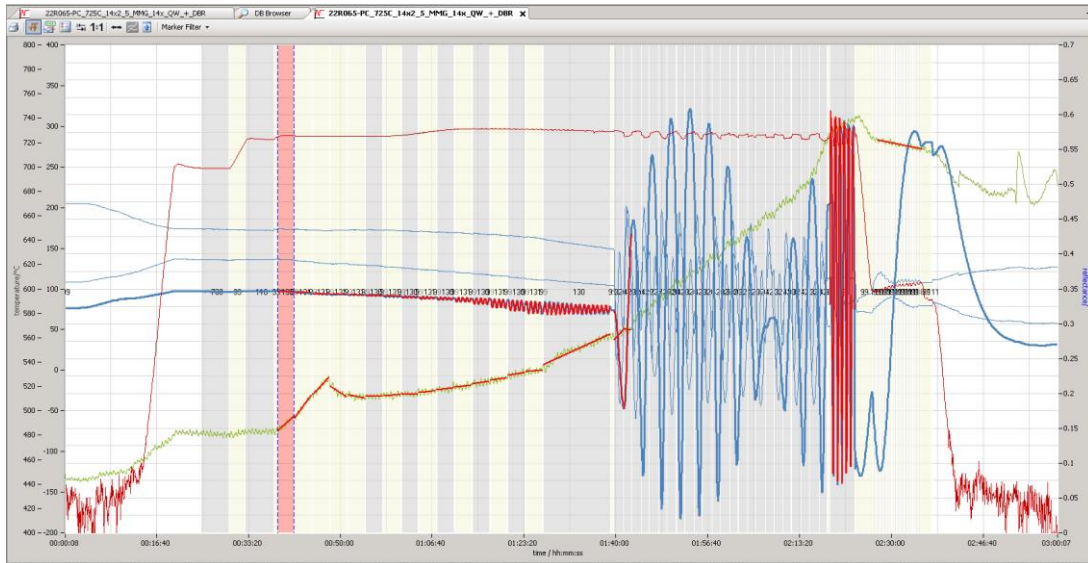


Figure 4.9 Growth Telemetry of DBR containing photocathode (run # 22R065).

Initial DBRs were grown, and the telemetry of these growths is shown Figure 4.9. As the telemetry shows, the reflectivity measurements during the DBR growth oscillate rapidly. This is because a DBR is designed explicitly to reflect light so as the DBR layers are grown, an increase in these oscillations is expected [46].

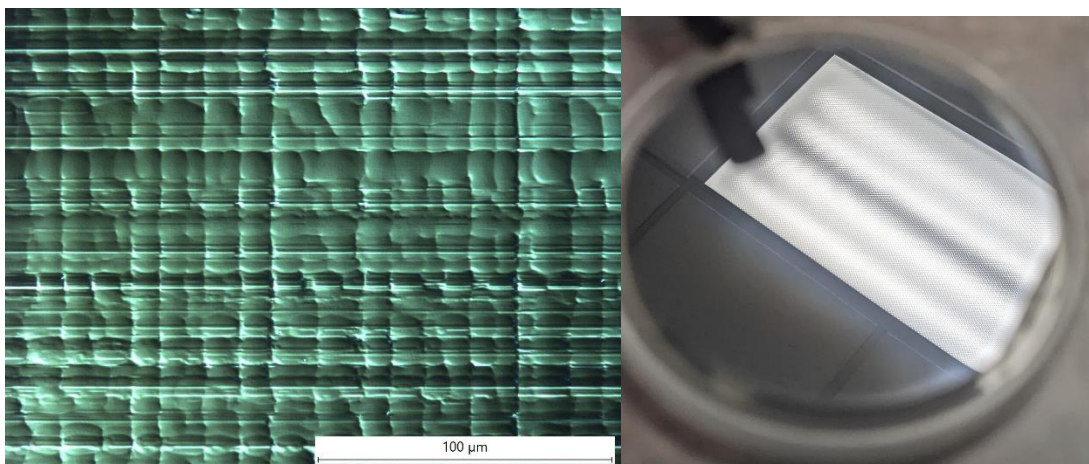


Figure 4.10 Nomarsky image and optical image of Photocathode with DBR (run 22R065).

Examining the Nomarski of the completed growth surface (Figure 4.10), there is a significant degree of texturing, but it is highly periodic. Unlike the device without the DBR, the Nomarski shows additional lateral lines along the surface. These lines indicate a potential lattice mismatch between the DBR material and the buffer. Examining the curvature during DBR growth, the positive slope implies that the DBR was grown tensile, which reinforces the potential presence of lattice mismatch. While there are some indicators of lattice mismatch within the DBR, the photocathode surface is highly specular under optical examination.

To analyze the quality of DBR both TEM and reflectivity measurements were performed. Reflectivity measurements (Figure 4.11) are particularly important because, unlike traditional mirrors, a DBR has a given bandwidth of high reflectivity and regions of significantly lower reflectivity. A poorly tuned DBR could only have a marginal impact on Quantum efficiency and a properly tuned one could significantly improve device properties.

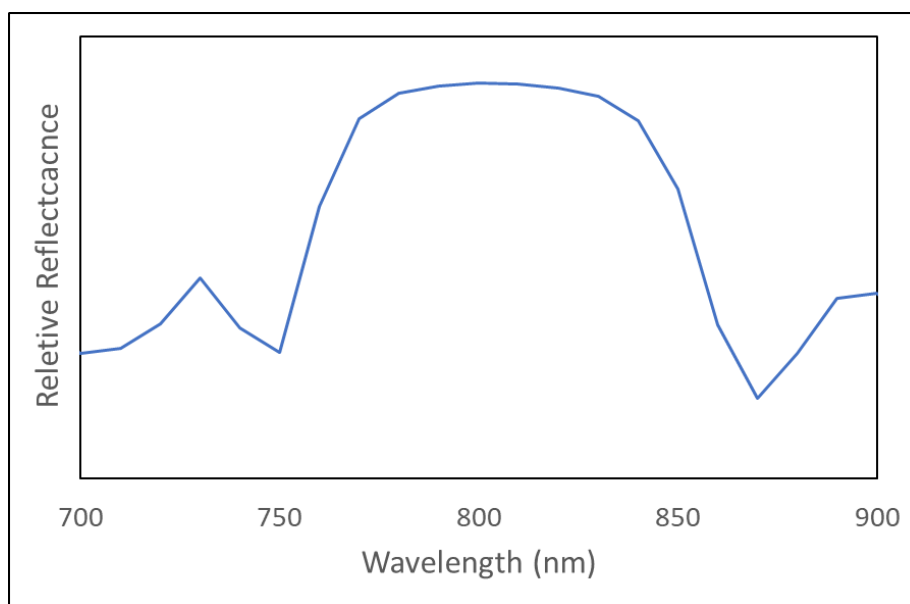


Figure 4.11 Reflectivity measurement as a function of wavelength for a DBR deposited on a metamorphic layer

Figure 4.11 shows a test DBR grown for device 22R065. On the DBR described above, a finished photocathode was grown and characterized. Figure 4.12 shows the comparison of the QE and

spin polarization of a photocathode with the same strained superlattice recipe with and without a DBR (r). By comparing the two, it is possible to examine how the DBR can impact depolarization.

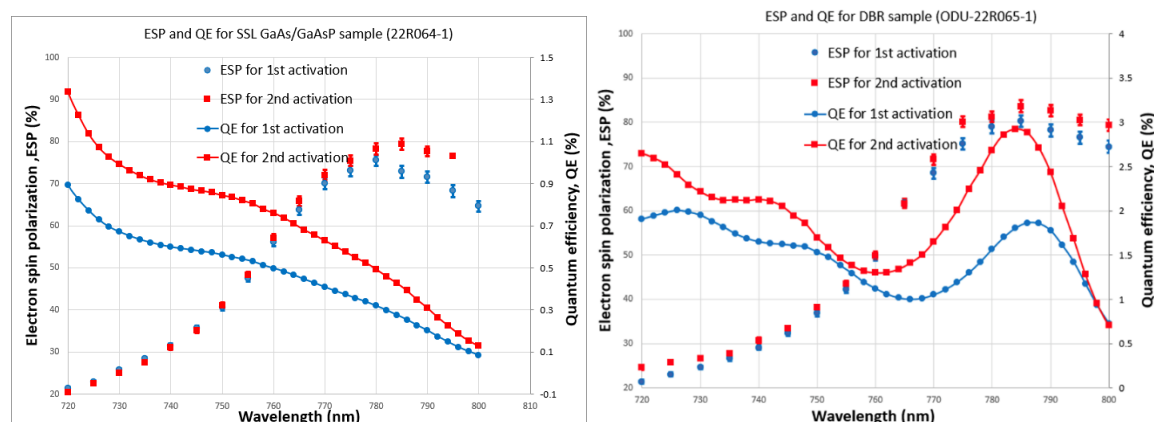


Figure 4.12 Two different photocathodes with the same superlattice recipe without DBR (22R064, Left) and with DBR (22R065, right).

As Figure 4.12 shows, the location of peak polarization is the same for both photocathodes, but the DBR has a significant impact on the quantum efficiency. The resulting figure of merit with a value of 2 is the second best reported of all photocathodes as of today, with the best reported values for MOCVD grown photocathodes.

Table 3 Photocathode Results compared to other works

Cathode Structure	Reference	P(%)	QE(%)	P ² QE(%)
GaAsGaAsP _{0.36}	SLAC/SVT [47]	86	1.2	0.89
GaAs-GaAsP _{0.38}	Nagoya [48]	92	1.6	1.35
Al _{0.19} In _{0.20} GaAs-Al _{0.40} GaAs	St. Petersburg [49]	92	0.85	0.72
GaAs-GaAsP _{0.35} (DBR)	JLAB/SVT [4]	84	6.4	4.52
GaAs-GaAsP _{.35}	22R064	80	0.3	0.19
GaAs-GaAsP _{0.35} (DBR)	22R065	82	2.9	1.95

As Table 3 shows, our photocathode (run # 22R065) is the second-best photocathode ever reported. It should also be noted that the other growths reported in Table 3 were done exclusively via MBE while the growths done for this work were via MOCVD.

While this result is exciting, additional work can be done to refine the quality of these photocathodes. While the initial DBR showed promising results, additional work can be done to

optimize it. Since the non-DBR and DBR samples were grown in parallel, the bandwidth of the DBR was left intentionally broad to ensure that the point of peak polarization was in a region of high reflectivity. Now that the point of peak polarization is known, the DBR can be further optimized to further increase reflectivity within the area of interest.

One other area of interest discussed previously is potential strain within the DBR. Ideally, the DBR should be lattice matched to the GaAsP buffer layer. If this is not the case, then dislocations could form within the DBR and these dislocations could have a detrimental impact on both the DBR and the superlattice (Figure 4.13).

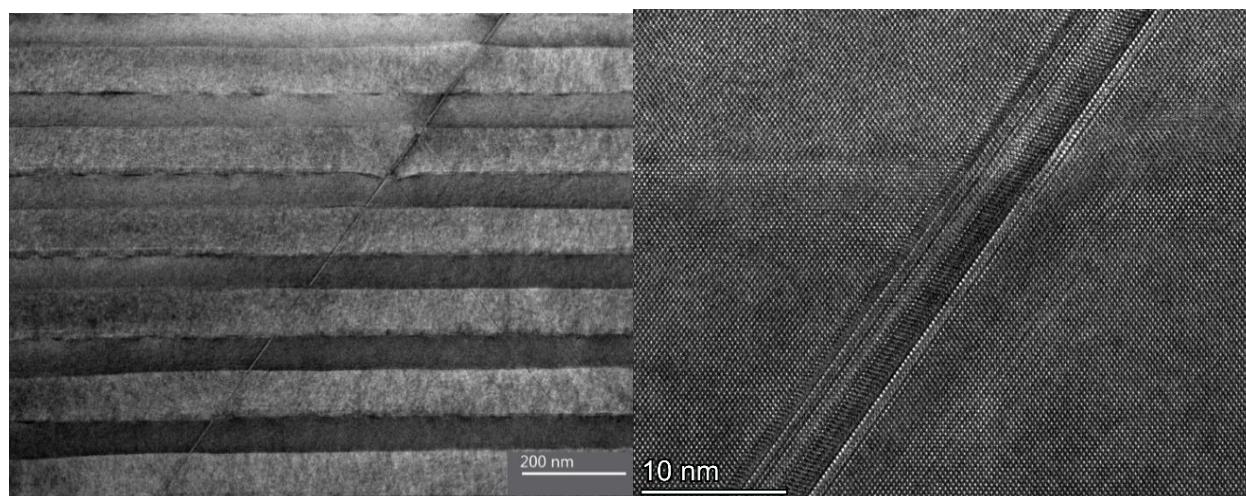


Figure 4.13 TEM imaging of the DBR from the previously reported device with additional magnification on the dislocation (22R065)

Figure 4.13 shows the DBR of the photocathode reported in Figure 4.12 (22R065). While the layers are highly periodic, they are not defect free. This is because the DBR itself had miscalibration in the In/Al fraction of the InAlP layer. Because these layers were on the order of 10s of nanometers thick, the critical thickness was surpassed, and defects were able to form. Figure 4.14 shows the stacking fault in more detail. Compared to a simple thread dislocation, a stacking fault is a full planar defect within the grown structure. For GaAs, these stacking faults typically follow the (111) burger vector at 60°. These stacking faults can be extremely problematic because

they will propagate into the superlattice. If they do propagate into the superlattice, they will cause sites for electron recombination thus lowering quantum efficiency.

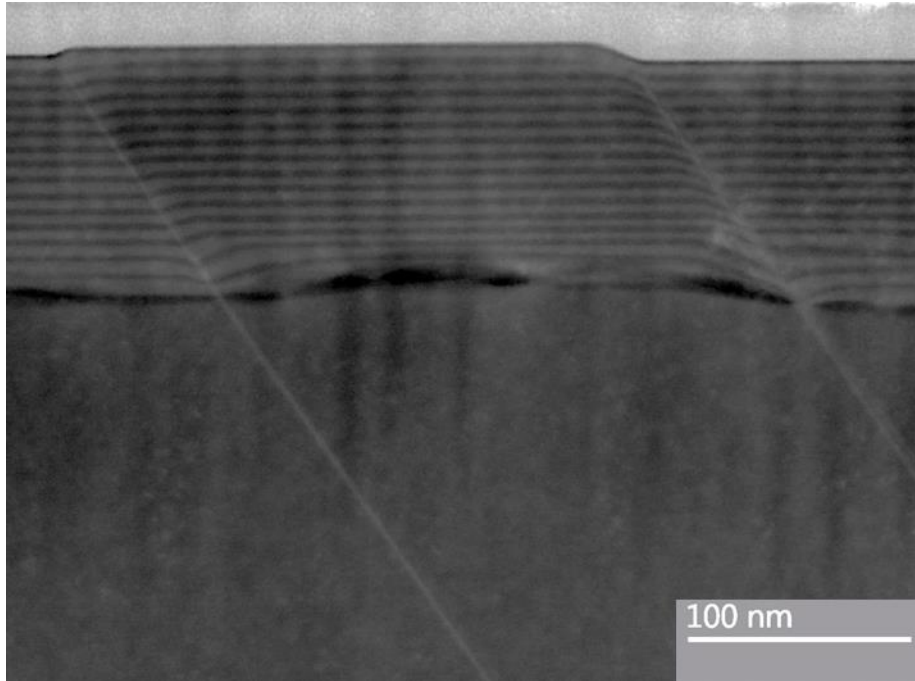


Figure 4.14 Impact of misfit dislocation caused by lattice mismatch in the DBR propagating into the superlattice (run22R065)

Figure 4.14 shows the impact of these threading dislocations within the super lattice. At the sites of these dislocations, the layers within the superlattice become compressed, which changes the polarization since the threads are running diagonal through the superlattice. This can cause potential recombination sites limiting diffusion of electrons from the surface. By decreasing the lattice mismatch within the DBR, device performance can further be increased.

Conclusion

Development of MOCVD-based spin polarized photocathodes are integral to increasing the supply of these devices. While their applications are currently limited to accelerator physics applications, once these devices are more readily available, additional applications over various fields will be open. Until this work, the main source of high-quality photocathodes were from MBE. While MBE can produce high quality photocathodes, scale up to more industrial applications with MBE is not necessarily feasible.

In this work, starting from designs from previously MBE-grown photocathodes, strained superlattice photocathodes were grown via MOCVD. This was done over multiple phases to address the differences in deposition processes between MBE and MOCVD. A significant portion of time was spent developing high-quality relaxed tensile buffers. After these buffers were developed, refinement of the superlattice resulted in spin polarizations greater than 80%. Finally a DBR implementation resulted in the second best reported P²QE photocathode and the best reported via MOCVD.

A framework for continued development was also developed for further refinement of distributed Bragg reflector and strain compensated superlattice development. With the creation of highly reproducible spin polarized photocathodes via MOCVD, a source for spin polarized positrons for various new scientific and characterization applications might be accessible.

References

- [1] A. Opper, Measuring the weak charge of the proton at Jefferson Lab: A search for physics beyond the standard model. *Few-Body Syst* **44**, 23–25 (2008).
- [2] K. Koike, Spin-polarized scanning electron microscopy, *Microscopy*, Volume 62, Issue 1, February 2013, Pages 177–191.
- [3] D. Abbott, P. Adderley, A. Adeyemi, P. Aguilera, M. Ali, H. Areti, M. Baylac, J. Benesch, G. Bosson, B. Cade *et al.* "Production of Highly Polarized Positrons Using Polarized Electrons at MeV Energies", *Phys. Rev. Lett.* 116, 214801 (2016).
- [4] W. Liu, Y. Chen, W. Lu, A. Moy, M. Poelker, M. Stutzman, *and* S. Zhang, "Record-level quantum efficiency from a high polarization strained GaAs/GaAsP superlattice photocathode with distributed Bragg reflector", *Appl. Phys. Lett.* 109, 252104 (2016).
- [5] T. Maruyama, E. L. Garwin, R. Prepost, and G. H. Zapalac, "Electron-spin polarization in photoemission from strained GaAs grown on GaAs_{1-x}P_xGaAs_{1-x}P_x," *Phys. Rev. B* 46(7), 4261–4264 (1992).
- [6] R. Prepost and T. Maruyama, "Advances in Polarized Electron Sources", *Annual Review of Nuclear and Particle Science* 1995 45:1, 41-88.
- [7] W. Rindner and Ernest Pittelli , "Effects of Stress-Induced Band-Gap Widening and Defects in GaAs Junctions", *Journal of Applied Physics* 37, 4437-4439.
- [8] T. Maruyama, E. L. Garwin, R. Prepost, G. H. Zapalac, J. S. Smith, and J. D. Walker, Observation Of Strain-Enhanced Electron-Spin Polarization In Photoemission From InGaAs, *Phys. Rev. Lett.* 66.
- [9] P. J. Orders and B. F. Usher , "Determination of critical layer thickness in In_xGa_{1-x}As/GaAs heterostructures by x-ray diffraction", *Appl. Phys. Lett.* 50, 980-982.

- [10] T. Omori, Y. Kurihara, Y. Takeuchi, M. Yoshioka, T. Nakanishi, S. Okumi, M. Tsubata, M. Tawada, K. Togawa, Y. Tanimoto, C. Takahashi, T. Baba, and M. Mizuta, "Highly Polarized Electron Source Using InGaAs-GaAs Strained-Layer Superlattice", *Jpn. J. Appl. Phys., Part 1* 33, 5676.
- [11] G. Rajan, S. Karki, R. W. Collins, N. Podraza, and S. Marsillac, "Real-Time Optimization of Anti-Reflective Coatings for CIGS Solar Cells". *Materials*, 13(10): 4259.
- [12] R. E. Welser, S. J. Polly, A. K. Sood, S. M. Hubbard and K. H. Montgomery, "Epitaxial Reflector Structures for High Efficiency Quantum Well Solar Cells," *2019 IEEE 46th Photovoltaic Specialists Conference (PVSC)*, 2019, pp. 2642-2645.
- [13] A. G. Zhuravlev, V.S. Khoroshilov, and V. L. Alperovich. Electron emission from Cs/GaAs and GaAs(Cs, O) with positive and negative electron affinity. *Jetp Lett.* 105, 686–690.
- [14] A. Y. Cho, J. R. Arthur, "Molecular Beam Epitaxy", *Progress in Solid State Chemistry*, 10(3), 157-191.
- [15] N. Chand, T. D. Harris, S. N. G. Chu, E. A. Fitzgerald, J. Lopata, M. Schnoes, and N.K. Dutta, "Performance of a valved arsenic cracker source for MBE growth". *Journal of Crystal Growth*, 126(4): 530-538.
- [16] A. G. Thompson. "MOCVD technology for semiconductors", *Materials Letters* 30(4) 255-263.
- [17] J. W. Matthews and A. E. Blakeslee "Defects in epitaxial multilayers: 1: Misfit dislocations". *Journal of Crystal Growth* 27 118-125.
- [18] Bett, A., Dimroth, F., Stollwerck, G. *et al.* III-V compounds for solar cell applications. *Appl Phys A* 69, 119–129.
- [19] G. H. Olsen., "Interfacial lattice mismatch effects in III-V compounds", *Proceedings of the Third International Conference on Vapour Growth and Epitaxy*, 1975 223-239.
- [20] Irvine, S. and Capper, P. (2019). Introduction to Metalorganic Vapor Phase Epitaxy. In *Metalorganic Vapor Phase Epitaxy (MOVPE)* (eds S. Irvine and P. Capper).

- [21] M. A. Steiner *et al.*, "2.0–2.1 eV Ga_xIn_{1-x}P solar cells grown on relaxed GaAsP step grades," *2010 35th IEEE Photovoltaic Specialists Conference*, 2010, pp. 002111-002116.
- [22] K. Haberland, A. Kaluza, M. Zorn, M. Pristovsek, H. Hardtdegen, M. Weyers, J.-T. Zettler, W. Richter., "Real-time calibration of wafer temperature, growth rate and composition by optical in-situ techniques during Al_xGa_{1-x}As growth in MOVPE", *Journal of Crystal Growth*, Volume 240, Issues 1–2, 2002, Pages 87-97.
- [23] J.F. Geisz, A.X. Levander, A.G. Norman, K.M. Jones, M.J. Romero, "In situ stress measurement for MOVPE growth of high efficiency lattice-mismatched solar cells", *Journal of Crystal Growth*, Volume 310, Issues 7–9, 2008, Pages 2339-2344,
- [24] W. Lang. *Nomarski differential interference-contrast microscopy*. Oberkochen: Carl Zeiss, 1982.
- [25] B. Belfore, D. Poudel, S. Karki, S. Soltanmohammad, E. Palmiotti, T. Lepetit, A. Rockett, S. Marsillac, Recrystallization of Cu(In,Ga)Se₂ Semiconductor Thin Films via InCl₃ Treatment, *Thin Solid Films*, Volume 735, 2021.
- [26] S. A. Speakman. "Introduction to high resolution x-ray diffraction of epitaxial thin films." *MIT Center for Materials Science and Engineering, Cambridge* (2012).
- [27] P. F. Fewster. "Reciprocal space mapping." *Critical Reviews in Solid State and Material Sciences* 22.2 69-110.
- [28] T. Begou, J. D. Walker, D. Attygalle, V. Ranjan, R. W. Collins, and S. Marsillac, Real time spectroscopic ellipsometry of CuInSe₂: Growth dynamics, dielectric function, and its dependence on temperature. *Phys. Status Solidi RRL*, 5: 217-219.
- [29] S. Marsillac, M. N. Sestak, J. Li, and R. W. Collins, "Spectroscopic ellipsometry," in *Advanced Characterization Techniques for Thin Film Solar Cells* edited by D. Abou-Ras, T. Kirchartz, and U. Rau (Wiley-VCH, Weinheim, 2011), p. 125.
- [30] J. Zhang, J. Hwang, B. J. Isaac, and S. Stemmer. Variable-angle high-angle annular dark-field imaging: application to three-dimensional dopant atom profiling. *Sci. Rep.* 5, 12419.

- [31] C. Y. Chang, L. P. Chen, and C. H. Wu, "Investigation of zinc incorporation in GaAs epilayers grown by low-pressure metalorganic chemical-vapor deposition", *Journal of Applied Physics* 61, 1860-1863.
- [32] F. Ermanis and K. Wolfstirn, "Hall Effect and Resistivity of Zn-Doped GaAs", *Journal of Applied Physics* 37, 1963-1966.
- [33] J.L. McCarter, M. L. Sutzman, K. W. Trantham, T. G. Anderson, and A. M. Cook, "A low-voltage retarding-field Mott polarimeter for photocathode characterization," *Nucl. Instrum. Methods A*, 618 pp. 30-36.
- [34] O. Salehzadeh, C. He, W. Benyon, A.J. SpringThorpe, "The effects of zinc-doping on the composition of InGaAsP layers grown by MOCVD", *Journal of Crystal Growth*, Volume 445, Pages 110-114.
- [35] C. Y. Chang, L. P. Chen, and C. H. Wu, "Investigation of zinc incorporation in GaAs epilayers grown by low-pressure metalorganic chemical-vapor deposition", *Journal of Applied Physics* 61, 1860-1863.
- [36] C. R. Lewis, and M. J. Ludowise, "The compositional grading of MOCVD-grown GaAs_{1-x}P_x via substrate temperature changes". *J. Electron. Mater.* **13**, 749–761.
- [37] R. S. Goldman, K. L. Kavanagh, H. H. Wieder, S. N. Ehrlich, and R. M. Feenstra, "Effects of GaAs substrate misorientation on strain relaxation in In_xGa_{1-x}As films and multilayers." *Journal of Applied Physics* 83(10): 5137-5149.
- [38] T. E. Haynes, W. K. Chu, L. Aselage, and S. T. Picraux, "Initial decomposition of GaAs during rapid thermal annealing", *Appl. Phys. Lett.* 49, 666-668.
- [39] W. Liu, M. Poelker, X. Peng, S. Zhang, and M. Stutzman, "A comprehensive evaluation of factors that influence the spin polarization of electrons emitted from bulk GaAs photocathodes", *Journal of Applied Physics* 122, 035703.
- [40] G. L. Bir, A. G. Aronov, and G. E. Pikus, *Zh. Eksp. Teor. Fiz.* 69, 1382 (1975) [*Sov. Phys. JETP* 42, 705 (1975)]

- [41] A. Bougoffa, A. Trabelsi, A. Zouari, and E. Dhari. Analysis of external quantum efficiency and conversion efficiency of thin crystalline silicon solar cells with textured front surface. *J Comput Electron* **15**, 1085–1094.
- [42] G. Rajan, A. R. Ibdah, K. Aryal, T. Ashrafee, V. Ranjan, E. A. Pogue, A. Rockett, R. W. Collins, and S. Marsillac, Optical enhancement of ultra-thin CIGS solar cells using multi-layered antireflection coatings. In *2014 IEEE 40th Photovoltaic Specialist Conference (PVSC)* (pp. 1687-1690). IEEE.
- [43] R. E. Welser, S. J. Polly, A. K. Sood, S. M. Hubbard and K. H. Montgomery, "Epitaxial Reflector Structures for High Efficiency Quantum Well Solar Cells," *2019 IEEE 46th Photovoltaic Specialists Conference (PVSC)*, 2019, pp. 2642-2645,
- [44] G. Guisbiers, M. Wautelet, and L. Buchailot "Phase diagrams and optical properties of phosphide, arsenide, and antimonide binary and ternary III-V nanoalloys", *Phys. Rev. B*, 79 (2009), p. 155426,
- [45] A. Addamiano, "On the preparation of the phosphides of aluminum, gallium and indium." *Journal of the American Chemical Society* 82, no. 7 (1960): 1537-1540.
- [46] H. P. D. Schenk, P. de Mierry, P. Vennéguès, O. Tottereau, M. Laügt, M. Vaille, E. Feltin, B. Beaumont, P. Gibart, S. Fernández, and F. Calle, "In situ growth monitoring of distributed GaN–AlGaIn Bragg reflectors by metalorganic vapor phase epitaxy", *Appl. Phys. Lett.* 80, 174-176 (2002).
- [47] T. Maruyama, D. A. Luh, A. Brachmann, J. E. Clendenin, E. L. Garwin, S. Harvey, J. Jiang, R. E. Kirby, C. Y. Prescott, R. Prepost, and A. M. Moy, *Appl. Phys. Lett.* 85, 2640 (2004).
- [48] X. G. Jin, B. Ozdol, M. Yamamoto, A. Mano, N. Yamamoto, and Y. Takeda, *Appl. Phys. Lett.* 105, 203509 (2014).
- [49] A. Yu. A Mamaev, L. G. Gerchikov, Yu. P. Yashin, D. A. Vasiliev, V. V. Kuzmichev, V. M. Ustinov, A. E. Zhukov, V. S. Mikhrin, and A. P. Vasiliev, *Appl. Phys. Lett.* 93, 081114 (2008).

Benjamin T. Belfore

*Department of Electrical and Computer Engineering
Old Dominion University, Norfolk, VA
Email: bbelf001@odu.edu Phone: 757-771-5919*

Education

PhD Electrical Engineering, Old Dominion University (2017-Present) GPA: 3.87

BS Chemical Engineering Virginia Polytechnic Institute and State University (2012-2016)

Areas of Expertise

- **Microfabrication:** Photolithography, Metallization, Spin Coating, Etching, Lift-Off
- **Characterization:** HRXRD, XPS, SEM, SIMS, Spectroscopic Ellipsometry, Profilometry, XRF, EDS, AFM
- **Thin Film Deposition:** DC/RF Sputtering, Thermal co-evaporation, e-beam evaporation, chemical bath deposition, MOCVD
- **Software:** KLayout, COMSOL, MATLAB, SCAPS, LABVIEW, Minitab, Autodesk Inventor, AutoCAD, ASPEN Plus, PSpice, MultiSIM, NetLOGO
- **Numerical Modeling:** Finite Element Analysis Agent-based Modeling

Experience

- **Class 1000 Cleanroom Laboratory Manager (VIPV)**
Department of Electrical and Computer Engineering, Old Dominion University (2019-Present)
 - Responsible for maintaining the quality of a class 1000 cleanroom
 - Extensive experience in the use of and teaching of in the fundamental manufacturing steps for microelectronic devices (MOSFET, MOS diodes, and capacitors) from fundamental process steps including photolithography, wet etching, oxidation, diffusion, and metallization
 - Procure materials to ensure the continuous operation of research equipment
 - Redesigned undergraduate course to utilize new maskless aligner
 - Act as primary contact with vendors to procure goods and equipment
 - Manage budgets and work with companies and university officials
- **Graduate Research & Teaching Assistant, Virginia Institute of Photovoltaics**
Department of Electrical and Computer Engineering, Old Dominion University (2017-Present)

Projects Involved

- Development of Spin Polarized Photocathodes for Particle Accelerators, US Department of Energy (2020-Present).
- Modeling Dynamic Recrystallization of Phase Change Materials for Applications in Adaptive Optics, NASA (2020-Present)
- Post-Growth Recrystallization by Halides for High Throughput CIGS Photovoltaics, US Department of Energy (2016-2021)
- Understanding of Module-level Light-, Moisture- and Thermal-Induced Instabilities in CIGS Photovoltaics, US Department of Energy (2017-2019)
- 5 years of hands-on experience with PVD equipment with multiple applications
- Assist in the writing of Grant Proposals, continuation reports, and contract meetings for multiple concurrent projects
- Mentoring of junior graduate students (6) and undergraduate students (8) to design, conduct, and complete independent research projects
- Directly responsible for the repairs and upgrades of multiple physical vapor deposition systems

- Coordinated between multiple governmental and university organizations to reach key research milestones
- Oversaw implementation of growth optimization of MOCVD growths for spin polarized photocathodes
- Optimized growth parameters to improve efficiency for rapidly-deposited low temperature solar cells
- Assist junior graduate students in the implementation of various projects including sputtering of super conducting Niobium thin films, reactive sputtering of III-nitride semiconductors, photomask design of logic gates, and trapped ion quantum computing
- **Undergraduate Highlights**
 - Work with export-controlled (EAR) materials in a private military contractor environment and perform FMEA and HAZOP for high-risk environments (Radford Army Ammunition Plant)
 - Work with small scale industry level equipment including: batch distillation, continuously stirred tank reactors, hydrogen fuel cells, fermenters, membrane separators, gas absorption columns, and rotary drum filtration

Honors/Awards

- Virginia Space Grant Consortium Research Fellow (2020-Present)
- Outstanding Graduate Teaching Assistant Award (2019)
- NSF SoLEAP Scholar (2018-2019)
- Faculty Emeriti Klinefelter/Phillips Scholar (2018-2020)

Professional Memberships

- IEEE Student Member
- ASQ Student Member
- AIChE Graduate Member

Publication Highlights

- **A total of 24 Journal Articles and Conference Proceedings Published (additional ones pending) full list available upon request.**
- **Publication Highlights**
 - Belfore B. *et al.* (2021) "Recrystallization of Cu (In, Ga) Se₂ Semiconductor Thin Films via InCl₃ Treatment" *Thin Solid Films*, 735, 138897.
 - Rajan G. *et al.* (2019) "Impact of Post-Deposition Recrystallization by Alkali Fluorides on Cu(In,Ga)Se₂ Thin Film Materials and Solar Cells" *Thin Solid Films*, 690, 137526.
 - Karki S. *et al.* (2019) "Degradation Mechanism in CIGS Material and Solar Cells Due to Moisture and Heat Treatment of the Absorber Layer" *IEEE Journal of Photovoltaics*, 9(4), 1138-1143.
 - Belfore B. *et al.* (2019) "Modeling Diffusion of Impurities in Molybdenum Thin Films as a Function of Substrate Temperature" *IEEE Journal of Photovoltaics*, 9(1), 339-343.
 - Karki S. *et al.* (2019) "Analysis of Recombination Mechanisms in RbF-Treated CIGS Solar Cells" *IEEE Journal of Photovoltaics* 9 (1) 313-318.